



1 **Tropical upper tropospheric trends in ozone and carbon** 2 **monoxide (2005–2020): observational and model results**

3 Lucien Froidevaux¹, Douglas E. Kinnison², Benjamin Gaubert², Michael J. Schwartz¹, Nathaniel

4 J. Livesey¹, William G. Read¹, Charles G. Bardeen², Jerry R. Ziemke^{3,4}, and Ryan A. Fuller¹

5 ¹Jet Propulsion Laboratory, California Institute of Technology, Pasadena, California, USA

6 ²NSF National Center for Atmospheric Research (NSF NCAR), Boulder, Colorado, USA

7 ³NASA Goddard Space Flight Center, Greenbelt, MD, USA

8 ⁴Goddard Earth Sciences Technology and Research (GESTAR)/Morgan State University,

9 Baltimore, MD, USA

10 *Correspondence to:* Lucien Froidevaux (lucienf@jpl.nasa.gov)

11 **Abstract.** We analyze tropical ozone (O₃) and carbon monoxide (CO) distributions in the upper
12 troposphere (UT) and their temporal changes for 2005–2020 using Aura Microwave Limb Sounder
13 (MLS) observations and chemistry climate models. The models are the Whole Atmosphere
14 Community Climate Model (WACCM6) and two variants of the Community Atmosphere Model
15 with Chemistry (CAM-chem), each variant using different anthropogenic emissions. Upper
16 tropospheric trends and variability diagnostics are obtained from multiple linear regression
17 analyses. We compare the model and MLS annual climatologies, focusing on 147 and 215 hPa
18 pressure levels; climatological values generally fall within 10–20% of each other, with both
19 positive and negative differences for O₃, and with models generally underestimating observed CO.
20 In the northern hemisphere tropics, we find significantly poorer model fits to the observed phasing
21 of CO seasonal changes at 215 hPa than at 147 hPa. This discrepancy is much smaller for the
22 comparison of modeled and Measurements of Pollution in the Troposphere (MOPITT) V9J CO
23 columns. We also find that the sensitivity of UT CO to El Niño / Southern Oscillation (ENSO) is
24 positive at all tropical longitudes, in contrast to the dipolar longitudinal structure that exists for UT
25 O₃ ENSO sensitivity.

26 MLS O₃ has a zonal mean trend at 20°S–20°N of $+0.39 \pm 0.28$ %yr⁻¹; CAM-chem and WACCM
27 have similar trends, though the WACCM trend is somewhat smaller. Our analyses for specific
28 latitude/longitude bins yield positive trends up to 1.4 %yr⁻¹ over Indonesia and East of that region,
29 as well as over tropical Africa and the tropical Atlantic. We find broad similarities between the
30 mapped MLS-derived UT O₃ trends and corresponding mapped trends of tropospheric column
31 ozone. Positive tropical UT mapped O₃ trends are generally captured by the models, although in a



32 more muted way. There is room for improvements in modeled tropical UT CO trends. Indeed, the
33 MLS zonal mean CO trend is $-0.25 \pm 0.30 \text{ \%yr}^{-1}$, whereas the corresponding modeled CO trends
34 are near zero ($0.0 \pm 0.14 \text{ \%yr}^{-1}$) when the anthropogenic emissions used in CAM-chem and
35 WACCM are taken from Community Emissions Data System (CEDS) version 2. The non-CEDS
36 version of CAM-chem yields CO UT trends of $0.22 \pm 0.19 \text{ \%yr}^{-1}$, in contrast to the negative MLS
37 CO trends throughout the tropics. The negative MLS tropical UT CO trends for 2005–2020 agree
38 with (but tend to be smaller in magnitude than) previously published total column CO trends.
39 Decreasing CO emissions from anthropogenic and biomass burning sources have previously been
40 suggested as the main causes of tropospheric CO decreases, although significant regional emission
41 trend variations exist.

42 **1 Introduction**

43 Tropospheric ozone (O_3) can be influenced by downward transport from the stratospheric ozone
44 layer, but the main O_3 source in the troposphere is in situ photochemical formation through the
45 oxidation of carbon compounds in the presence of (catalyzing) nitrogen oxides ($\text{NO}_x = \text{NO} + \text{NO}_2$)
46 (Crutzen, 1973; Logan, 1985); tropospheric ozone loss is dominated by in situ photochemistry and
47 by deposition at the Earth's surface (Monks et al., 2015). Past studies have also shown that the
48 main sources of tropospheric NO_x are fossil fuel combustion, biomass burning, soil microbial
49 activity, and lightning. Global anthropogenic emissions dominate the natural NO_x sources and
50 biomass burning plays quite a significant role in the tropics. There is evidence from in situ
51 measurements from ozonesondes and commercial aircraft for slow increases in tropospheric and
52 upper tropospheric O_3 abundances (e.g., Cooper et al., 2014; Gaudel et al., 2020; Thompson et al.,
53 2021; Wang et al., 2022). At the surface, regional differences have been noted, for example, a
54 leveling off in ozone increases over western Europe and parts of the United States after the 1990s,
55 including some decreases, depending on the season, with changes in ozone precursor emissions a
56 likely cause. Changes in tropospheric ozone precursor emissions (e.g., from NO_x , carbon
57 monoxide (CO), and volatile organic compounds) have been implicated as causes for global
58 tropospheric ozone change over the past few decades (Zhang et al., 2016; Zheng et al., 2018; Liu
59 et al., 2022; Wang et al., 2022). Souri et al. (2017) and Zhang et al. (2020), for example, discussed
60 the existence of decreases in NO_x emissions over some parts of the world after the turn of the
61 century. Furthermore, after the dramatic reduction in global economic activity following the



62 CO₂ CoronaVirus Disease 2019 pandemic, significant reductions in northern hemisphere (NH)
63 tropospheric ozone values were observed in 2020 and 2021, although the tropical decreases are
64 much smaller (Ziemke et al., 2022; Steinbrecht et al., 2021; Bouarar et al., 2021; Miyazaki et al.,
65 2021).

66 Carbon monoxide (CO) is another important pollutant in the troposphere. Its primary
67 tropospheric sources are incomplete combustion (pollution from industrial and traffic-related
68 emissions), the oxidation of methane and other hydrocarbons, and biomass burning emissions
69 (Logan et al., 1981; Crutzen and Andreae, 1990; Khalil and Rasmussen, 1990); its main
70 tropospheric loss pathway is oxidation by the hydroxyl radical (OH). A combination of Aura
71 Microwave Limb Sounder (MLS) and other satellite data has shown (Schoeberl et al., 2006) that
72 lower tropospheric CO anomalies, primarily from biomass burning episodes near the equinoxes
73 (Duncan et al., 2003, 2007; Logan et al., 2008; Nassar et al., 2009; Livesey et al., 2013; Huang et
74 al., 2016), are propagated upward by convection and general ascent to produce a tropical “CO tape
75 recorder” . Additional insights into the transport of CO pollution into the upper troposphere and
76 lower stratosphere (UTLS) have been provided by Park et al. (2013), who examined satellite
77 measurements of CO, C₂H₆, C₂H₂, and HCN from the Atmospheric Chemistry Experiment Fourier
78 Transform Spectrometer (ACE-FTS) and CO from MLS. In the tropics, the clear signature of
79 semiannual maxima centered around April and October are observed, primarily over continental
80 regions (Africa, Indonesia, and South America), with connections to biomass burning and
81 convection patterns. A specified dynamics version of Whole Atmosphere Community Climate
82 (WACCM) was shown by those authors to reproduce seasonal and semi-annual variations in
83 prior hydrocarbons fairly well. The model was found to underestimate CO abundances in the
84 southern hemisphere subtropics during austral spring, possibly due to problems with modeled
85 surface emissions, vertical transport, and/or tropospheric OH concentrations. Park et al. (2021)
86 provided additional detailed analyses of CO pollution transport to the UTLS during and long after
87 the highly enhanced 2015 Indonesian fire season, using a combination of CO satellite data, as well
88 as model simulations, which generally showed slight underestimates of satellite-derived
89 tropospheric and stratospheric CO abundances.

90 In terms of tropospheric CO trends, Worden et al. (2013a) found global CO column decreases
91 of about -1.5 %yr⁻¹ over Europe, East Asia, and the United States, and Laken and Sahbaz (2014)
92 obtained a -0.6 %yr⁻¹ global trend from 2000–2010, based mainly on satellite data sets from the



93 Measurements of Pollution in the Troposphere (MOPITT) and the Atmospheric Infrared Sounder
94 (AIRS) (see also Warner et al., 2013). Buchholz et al. (2021) found a similar general behavior
95 using 2002–2018 gridded time series from MOPITT CO, AIRS, and other satellite instruments
96 with shorter data records; the global trend for this period is found to be $-0.5 \pm 0.3 \text{ \% yr}^{-1}$. They also
97 demonstrated that lower tropospheric CO has declined at a slower rate during the 2010 to 2018
98 sub-period. Hedelius et al. (2021) have also discussed MOPITT-inferred decreasing trends in
99 column CO for 2002–2017 and pointed out regional and temporal sensitivities; they noted that
100 decreases in CO emissions, obtained from the Emissions Database for Global Atmospheric
101 Research (EDGAR) version 4.3.2, do not always match column CO trend results from similar
102 regions of the globe. Ground-based in situ measurements of surface-level CO from the World
103 Meteorological Organization’s (WMO) Global Atmospheric Watch (GAW) network also indicate
104 that there has been a slowdown in the rate of decrease of CO after 2010, in comparison to the
105 2001–2010 decade (Patel et al., 2024). There is also a north-south interhemispheric difference in
106 the CO abundances (and total columns), along with faster rates of decrease in the northern
107 hemisphere. Also, it is well known that the tropical region has significant variability tied to the El
108 Niño / Southern Oscillation (ENSO), which impacts uncertainties in atmospheric constituent
109 trends in this region.

110 Analyses of in situ CO data from commercial aircraft that participate in the In-service Aircraft
111 for a Global Observing System (IAGOS, see Petzold et al., 2015) measurements have also
112 indicated decreasing trends from 1995 to 2013 in northern midlatitude UT CO, with some larger
113 trends (as high as -2 to -3 \% yr^{-1}) over eastern Asia (Cohen et al., 2018). Decreasing CO emissions
114 from anthropogenic and biomass burning sources appear to be the main cause of global
115 tropospheric CO decreases (Jiang et al., 2017), while secondary CO resulting from methane
116 oxidation is increasing (Gaubert et al., 2017). Some steeper CO decreases have been observed in
117 local extra-tropical near-surface data (Li and Liu, 2011; He et al., 2013; Yoon and Pozzer, 2014;
118 Gratz et al., 2015), apparently because of tighter air quality standards and reduced pollution from
119 industrial and traffic-related emissions. In the North Atlantic region, both surface CO and O₃ have
120 decreased; Kumar et al. (2013) show this for 2001–2011. These decreases have been attributed to
121 a decline in anthropogenic emissions from North America that more than compensate for emission
122 increases over parts of Asia.



123 There are interannual composition changes in the troposphere and in the UTLS associated with
124 ENSO (Chandra et al., 1998; Ziemke and Chandra, 2003; Nassar et al., 2009; Oman et al., 2011,
125 2013) and related sea surface temperature and pressure changes. It has long been known that this
126 important mode of climate variability that originates in the Pacific Ocean, with alternating warm
127 (El Niño) and cold (La Niña) phases, leads to disruptions in global circulation patterns, and has
128 impacts on fire and wetland emissions that affect tropospheric composition (Feely et al., 1987;
129 Jones et al., 2001; Sudo and Takahashi, 2001; Duncan et al., 2003; Doherty et al., 2006; Calvo et
130 al., 2010; Voulgarakis et al., 2015; Rowlinson et al., 2019). The upper troposphere is a complex
131 region where production of NO_x by lightning (Schumann and Huntrieser, 2007; Murray et al.,
132 2014), aircraft NO_x emissions (Wang et al., 2022), and stratosphere-troposphere exchange (STE)
133 (Sudo et al., 2003; Collins et al., 2003; Hegglin and Shepherd, 2009; Hess and Zbinden, 2013; Neu
134 et al., 2014) can significantly impact ozone concentrations; STE plays a larger role in the extra-
135 tropics than in the tropics (Hsu and Prather, 2014).

136 Tropical upper tropospheric profiles of O₃ and CO have been measured on a continuous daily
137 basis by the Microwave Limb Sounder on the Aura satellite, from a near-polar sun synchronous
138 orbit since late 2004. Here, we present results of trends and variability analyses of these data sets
139 (from 2005–2020), along with a similar treatment of UT O₃ and CO time series from two chemistry
140 climate models, a “specified dynamics” version of the Whole Atmosphere Community Climate
141 Model version 6 (WACCM6) and the Community Atmosphere Model with chemistry (CAM-
142 chem), both of which are configurations of the Community Earth System Model version 2.2
143 (CESM2.2). In Sect. 2, we describe the MLS data sets as well as the simulations used here. Section
144 3 focuses on the trend analysis methodology. In Sect. 4, we discuss the analysis results, as well as
145 areas of agreement or disagreement between models and observations, and place this in context of
146 past analyses.

147 **2 Observations, model simulations, and trend analysis methods**

148 For both MLS and the chemistry climate models, we analyze monthly averaged zonal mean
149 time series as well as monthly-averaged longitude/latitude binned time series. The models have
150 been designed to capture key dynamical and chemical processes well enough to be usefully
151 compared to the observations. We focus on a region that is somewhat below the tropopause, to



152 minimize potential effects from stratosphere-troposphere exchange and results that might depend
153 more on lower stratospheric rather than tropospheric change.

154 **2.1 Observations**

155 The Aura MLS observational dataset considered here is taken from sixteen full years (2005
156 through 2020) of global composition measurements, with about 3500 vertical profiles per day per
157 measured species. The MLS antenna performs scans of the atmospheric limb ahead of the Aura
158 satellite in its near-polar sun-synchronous orbit. MLS measures daytime and nighttime thermal
159 emission using microwave radiometers operating at frequencies near 118, 190, 240, and 640 GHz;
160 a 2.5 THz module measured OH during the early part of the mission. The 240 GHz radiometer
161 provides the standard O₃ and CO measurements. For an overview of the MLS measurement
162 technique, the reader is referred to Waters et al. (2006). Read et al. (2006) gave a description of
163 the simulated MLS forward model and related spectra. The MLS retrievals (Livesey et al., 2006)
164 use the optimal estimation approach (Rodgers, 2000); there is no assumption of atmospheric
165 homogeneity along the line of sight (see Livesey and Read, 2000), and the retrievals make use of
166 the MLS antenna's views along overlapping tangent rays during consecutive scans of the Earth's
167 limb. The specifics of MLS data characterization and data quality, along with estimated errors and
168 related information can be found in the documentation by Livesey et al. (2022).

169 Here, we have used the latest data version from MLS, labeled version 5.0 or v5. More
170 specifically, we use the binned MLS Level 3 data sets, with a latitude grid that includes the
171 equatorial bin (-2° to +2°) and the 44 other adjacent 4°-wide bins. In this work, we analyze both
172 monthly zonal mean series (based on monthly averages of binned 24-hr averaged fields) and a
173 longitude-gridded subset (see below) of these monthly mean series; the typical number of MLS
174 profiles in a monthly zonal mean 4° bin is on order 2400, and about 200 for each of the 12 mapped
175 (monthly) longitude/latitude bins. Prior to averaging the MLS data, the standard MLS data quality
176 screening criteria (Livesey et al., 2022) have been applied to all the O₃ and CO Level 2 profiles;
177 this screening removes only a very small fraction (typically of order a few percent or less) of the
178 retrieved profiles. In the troposphere and stratosphere, the MLS O₃ retrieval grid is defined by a
179 subset of the pressure levels given by $p(n) = 1000 \times 10^{-n/12}$ hPa, where n is the pressure level index
180 number; for CO, the grid is twice as coarse, meaning that $n/6$ is used as an exponent in the above
181 equation, rather than $n/12$. The bottom recommended levels for the O₃ and CO retrievals are at 261



182 and 215 hPa, respectively. Our tropical analyses will focus on results between 215 and 147 hPa,
183 in order to largely obtain upper tropospheric results, as more influence from the stratosphere occurs
184 as one gets closer to 100 hPa in the tropics. In the upper troposphere, the vertical resolution of the
185 O₃ and CO products is about 3 km and 5 km respectively (Livesey et al., 2022). In this region, the
186 single-profile precision (1 σ random uncertainty) is 20–30 ppbv for O₃ and 15–20 ppbv for CO.
187 For our analyses of monthly MLS averages, the relevant precision for O₃ and CO reduces to ~0.5
188 ppbv for 4° zonal means and ~2 ppbv for the gridded data using 30° longitude by 4° latitude bins.
189 In addition, the methodology used by the MLS team to assess the aggregate effects of estimated
190 errors in various input parameters, coupled with validation results (see Livesey et al., 2022), leads
191 to systematic uncertainty estimates (1 σ) of 5–12 ppbv and 15–25 ppbv for tropical upper
192 tropospheric O₃ and CO, respectively.

193 Following validation work on UT MLS O₃ and CO in the early few years since the Aura launch
194 (Livesey et al., 2008), studies of UT MLS O₃ by Livesey et al. (2013) focused on seasonal and
195 interannual variability and comparisons versus ozonesonde data. Despite sampling differences
196 between these measurement systems, the temporal patterns evident in the MLS UT O₃ data were
197 found to be generally well correlated with the *in-situ* data over different low latitude regions.
198 Distinct seasonality was evident in O₃ and CO (as well as MLS-derived ice water content) over
199 South America and South Africa. Other patterns such as the “wave one” pattern in tropical O₃ and
200 double peaks in O₃ variability over eastern equatorial Africa (with enhancements around May/June
201 and September to November) were discussed; for MLS UT CO, distinct seasonal behavior was
202 found, for example, in the northern hemisphere tropics, over Eastern Asia and across the Pacific
203 (see also Huang et al., 2012). Livesey et al. (2013) and Huang et al. (2014) discussed the
204 connection between emissions from intense fires over Indonesia in 2006 (following the El Niño-
205 related drought) and dramatic concomitant enhancements in UT CO (from MLS data) over this
206 region. This work has been expanded upon in analyses by Park et al. (2013, 2021) of the significant
207 and long-lasting impacts of more recent El Niño-related droughts and wildfires on tropospheric
208 and lower stratospheric CO abundances.

209 **2.2 Model simulations**

210 We use the Whole Atmosphere Community Climate Model version 6 (WACCM6) and the
211 Community Atmosphere Model with Chemistry (CAM-chem), both of which are components of



1212 the CESM2.2 (Danabasoglu et al., 2020). WACCM6 uses the “high-top” set of 70 model levels
1213 between the surface and the lower thermosphere (~140 km), while CAM-chem uses 32 layers
1214 (“low-top”) that stop in the middle of the stratosphere (~40 km). Both configurations run on a
1215 horizontal resolution that is 0.95° latitude x 1.25° longitude and share the same vertical grid in the
1216 troposphere, with a vertical resolution in the upper troposphere of about 1.2 km. Both CAM-chem
1217 and WACCM6 include the same representations of boundary layer processes, shallow convection,
1218 liquid cloud macrophysics, and cloud microphysics (Gettelman et al., 2019). Each model employs
1219 the same chemical mechanism processes (labeled TS1). The chemical scheme includes the O_x,
1220 NO_x, HO_x, ClO_x, and BrO_x families, along with CH₄ and its degradation products, as well as
1221 primary non-methane hydrocarbons and related oxygenated organic compounds (Emmons et al.,
1222 2020). Reaction rates follow the JPL Publication 19-5 recommendation (Burkholder et al., 2019).
1223 TS1 includes a total of 231 species and 583 chemical reactions broken down into 150 photolysis
1224 reactions, 403 gas-phase reactions, 13 tropospheric, and 17 stratospheric heterogeneous reactions.
1225 The photolytic reactions are based on both inline chemical modules and a lookup table approach
1226 (Kinnison et al., 2007). Secondary organic aerosols are represented through the Volatility Basis
1227 Set approach (Tilmes et al., 2019). Comparisons of oxidants during the Korea–United States Air
1228 Quality (KORUS-AQ) experiment in South Korea led to a revision of the heterogeneous aerosol
1229 uptake of hydroperoxyl radicals (HO₂) to produce H₂O instead of H₂O₂ and a reduction of the
1230 coefficient (γ) from 0.2 to 0.1 (Gaubert et al., 2020).

1231 To accurately represent weather conditions as well as the Quasi-Biennial Oscillation (QBO)
1232 and to reproduce various modes of middle atmospheric variability, both simulations are run in the
1233 ‘specified dynamics’ (SD) mode. The model dynamical constraints are taken from meteorological
1234 fields provided by the Modern-Era Retrospective Analysis for Research and Applications version
1235 2 or MERRA-2 (Gelaro et al., 2017). Contrary to the previous SD approach, the MERRA-2 fields,
1236 here the zonal and meridional winds and temperature, are first regridded to the model horizontal
1237 and vertical grids. The model nudging (Davis et al., 2022) is updated at every (30 min) time step
1238 using the closest 3-hourly MERRA-2 fields; nudging timescales are set at 6 hours for the CAM-
1239 chem simulation and at 12 hours for WACCM6. The 11-year solar cycle variability is taken from
1240 the Naval Research Laboratory’s (NRL) solar model, namely the NRL Solar Spectral Irradiance
1241 version 2 (NRLSSI2; Coddington et al., 2016). Volcanic SO₂ emissions (used in sulfate aerosol
1242 density calculations) are derived for significant volcanic eruptions using the Neely and Schmidt



243 (2016) database updated through the year 2020. The model scenario used here is based on historical
244 forcings (and recent updates) from the Climate Model Intercomparison Project – Phase 6
245 (Meinshausen et al., 2017). The forcings include greenhouse gases (CH₄, N₂O, and CO₂) and
246 organic halogens. After 2014, the greenhouse gas and organic halogen inputs follow the CMIP6
247 SSP5-85 scenario that projects inputs beyond 2014 (O’Neill et al., 2016; Riahi et al., 2017;
248 Meinshausen et al., 2020).

249 The emissions from CMIP6 were updated to CAMS-GLOB-ANT_v5.1 in CAM-chem and
250 CAMS-GLOB-ANT_v5.3 in WACCM for all surface anthropogenic emissions (Soulié et al.,
251 2023). CO anthropogenic emissions were found to be too low in South Asia and China (Gaubert
252 et al., 2023), so these emissions were replaced by the Community Emissions Data System (CEDS)
253 v2, presented in McDuffie et al. (2020). Daily biomass burning emissions are obtained from the
254 Quick-Fire Emissions Dataset (QFED) 2.5 (Darmenov and da Silva, 2014) in both simulations. On
255 average, WACCM annual and tropical lightning NO_x emissions are 3.5 TgN yr⁻¹, a larger amount
256 than the 2.9 TgN yr⁻¹ from CAM-chem, but with no significant trends over the course of these
257 simulations. Aircraft emissions from CMIP6 were employed in WACCM. CAM-chem uses the
258 version 2.1 of CAMS-GLOB-AIR for aircraft emissions described by Soulié et al. (2023). Gaubert
259 et al. (2020, 2023) found that this version of CAM-chem tends to overestimate tropospheric
260 oxidants, such as ozone, hydrogen peroxide, nitric acid, and hydroxyl radical, resulting in a shorter
261 lifetime of tropospheric methane and CO, mainly in the northern hemisphere extra-tropics. Some
262 of the main model characteristics (with a focus on the differences) are summarized in Table 1.

263 In terms of the model run analyses, we follow the same basic approach as for the MLS data.
264 The daily model profiles are first interpolated (as a function of $\log(\text{pressure})$) onto the MLS
265 pressure grid and then binned and averaged to produce the monthly zonal means (on a 4° latitude
266 grid) and gridded data on the same latitude/longitude grid as is described in Sect. 2.1 for MLS.

267 **2.3 Trend analysis methods**

268 For both MLS and model time series trend analyses in the upper troposphere, we use the
269 multivariate linear regression (MLR) method discussed as part of similar studies performed by
270 Froidevaux et al. (2019) for the stratosphere. We refer the reader to Appendix (A3) of the above
271 reference for more details on the regression fit model, which includes commonly used functional
272 terms, namely a linear trend, cosine and sine functions with annual and semi-annual periodicities,



273 as well as functions describing variations arising from the QBO and ENSO. The QBO-related
274 equatorial wind dataset is obtained from the publicly available datasets at the Free University of
275 Berlin. ENSO-related data are in the form of a multivariate index, following the initial work of
276 Wolter and Timlin (2011), as updated by Zhang et al. (2019). We have also included a fitted
277 component that follows variations in solar radio flux (at 10.7 cm), based on Canadian solar
278 measurements (Tapping, 2013); this component typically plays a negligible role in our results. For
279 trend uncertainty estimates, as discussed also by Froidevaux et al. (2019, 2022), we use the block
280 bootstrap resampling method (Efron and Tibshirani, 1993), as done by Bourassa et al. (2014) and
281 others in such atmospheric composition analyses. For every fitted time series, we analyze
282 thousands of re-samplings of the fit residuals, with year-long blocks of residual values replaced by
283 residual series from randomly chosen years; twice the standard deviations in these random
284 distributions' trends provide the (2σ) trend uncertainty values that we use as trend error bars
285 throughout this work.

286 **3 Results**

287 **3.1 Climatologies**

288 Although this work focuses on variability and underlying trends, we start in Fig. 1 by showing
289 annually-averaged climatological ozone comparisons between MLS, CESM2 WACCM6 (simply
290 labeled WACCM), and CAM-chem-CEDS for 2005–2020 at 147 and 215 hPa for low latitudes
291 (4-degree bin centers between 24°S and 24°N); mapped fields and zonal mean line plots are
292 compared in this figure. At 215 hPa near 20°N and 20°S, the zonal mean O₃ values from both
293 models are ~5–10% lower than the MLS fields; differences of this order are also observed in the
294 mapped fields (and the percent difference fields). The differences reach about 20% in the deep
295 tropics, as the MLS latitudinal gradients are flat in this region, in contrast to the models' more
296 curved behavior, with a minimum at the equator (see panel (k)). The differences observed here are
297 within the MLS systematic uncertainties mentioned in Sect. 2.1 (up to 24 ppbv, 2σ). These two
298 models agree quite well in the UT region as a whole (typically within about 5 ppbv); such a good
299 level of agreement is not too surprising, given that these models are based on a very similar
300 framework, with nearly identical inputs (see Sect. 2.2). At smaller pressures (147 hPa and also for
301 100 hPa, which is not shown here), the models follow the MLS latitudinal gradients better (see



302 panel (d) for the comparison at 147 hPa), as well as the longitudinal features (including the well-
303 known wave-one ozone pattern discussed by Thompson et al., 2000, 2003, Wang et al., 2006, and
304 others). However, the models exhibit a positive average bias versus MLS at these two pressure
305 levels (see panel (e), where the model bias for 147 hPa is about +20%). We do not find that this
306 can be explained by using a vertically smoothed version of the model profiles, which more properly
307 takes into account the vertical resolution of the MLS observations, as the differences between
308 smoothed and unsmoothed zonal mean values are quite small in comparison to the model biases.
309 For simplicity, and for the above reasons, we have used unsmoothed model values in this work.
310 MLS UT O₃ profiles have been found to be biased positively (by up to about 20%) versus averaged
311 tropical ozonesonde profiles, based on sonde/MLS comparisons by Hubert et al. (2016) and from
312 our own comparisons. Thus, positive model biases versus MLS ozone in the tropical UT are not
313 likely caused by a significant underestimate by MLS. We also note that the positive model biases
314 (at 147 and 100 hPa) occur for all months of the year (not shown here), so this is not caused by a
315 very large bias in some months, that could be partially compensated for by negative model biases
316 in other months. Previous work has shown vertical oscillations in zonal mean MLS UTLS O₃
317 profiles (e.g., see Livesey et al., 2022); this could contribute to some of the mean differences
318 observed in Fig. 1. While there are some biases between modeled and MLS tropical ozone values,
319 these biases should not have a significant impact on the relative trend differences between these
320 models and MLS.

321 For CO, a similar set of annual mean climatological plots as those from Fig. 1 is provided in
322 Fig. 2. We observe that the model CO values follow the patterns of the MLS UT CO fields fairly
323 well, and the zonal mean model biases are usually less than 10–20%; the model biases are most
324 often negative, and more so in the northern tropics at 215 hPa. Again, it does not appear that
325 vertical smoothing of the models with MLS averaging kernels would account for the model/MLS
326 differences (see more details further below). The model CO UT biases shown in Fig. 2 are about
327 -5 to -15%, well within the MLS CO systematic uncertainties mentioned in Sect. 2.1; the CAM-
328 chem-CEDS climatological UT CO is slightly closer to the MLS UT CO climatology than is the
329 WACCM CO climatology. As in the case of ozone, the aforementioned model versus data CO
330 biases are found to exist not only for annual averages, but also on a month-to-month basis. The
331 SPARC Data Initiative report (SPARC, 2017) and the more recent update by Hegglin et al. (2021)
332 showed that MLS CO values in the tropical UT are within about 10–15% of the mean values that



333 include other data from ACE-FTS and the Michelson Interferometer for Passive Atmospheric
334 Sounding (MIPAS). However, the MLS mean values are larger than the multi-instrument mean at
335 100 hPa by about 10–20%, which can account for more than half of the MLS/model bias at this
336 level (not shown here). Also, just considering the theoretical systematic uncertainty estimates
337 provided in Sect. 2.1, it is possible that most (or even all) of the model/MLS bias at 100 hPa is
338 caused by a positive bias in the MLS CO data. However, an earlier WACCM version (WACCM4)
339 underestimated CO and other hydrocarbon data in the southern tropical UT, as described by Park
340 et al. (2013); those authors noted that model deficiencies in emission source strengths or in the
341 upward rate of transport could potentially explain these model underestimates. As mentioned
342 previously, we focus on the upper tropospheric region, somewhat removed from the tropopause,
343 with 147 to 215 hPa being the main levels of interest in the analyses below; while the UT average
344 differences between model and MLS are worth noting, this is not a primary concern in terms of
345 the trend comparisons that we focus on here.

346 **3.2 Zonal mean trends**

347 Regarding the trends, we now switch to results from our analyses of the monthly zonal mean
348 MLS and model time series. Figure 3 displays ozone trend results for MLS and the two models for
349 147, 178, and 215 hPa, based on a multiple linear regression analysis of the respective time series
350 from 2005 through 2020. Figure 3 shows that the tropical upper tropospheric MLS ozone trends
351 are positive and significant (at the 2σ level), with fairly small latitudinal differences at 215 hPa,
352 but at 147 hPa having ~50% larger trends in the NH tropics than in the SH tropics. The average
353 ozone trend for 2005–2020 in the 20°S – 20°N UT region is $0.39 \pm 0.28 \text{ \%yr}^{-1}$. The error bars here
354 indicate the 2σ trend uncertainty (we have used the rms of these from the three pressure levels in
355 Fig. 3). This tropical UT O_3 trend estimate is equivalent to $0.22 \pm 0.16 \text{ ppbv yr}^{-1}$ (based on the
356 annual average tropical UT values of 56 ppbv measured by MLS). The model O_3 zonal mean trend
357 results obtained here for 2005–2020 have a positive trend, with excellent agreement with MLS
358 from CAM-chem-CEDS ($0.38 \pm 0.28 \text{ \%yr}^{-1}$). There is also good statistical agreement with the
359 somewhat smaller WACCM average trends ($0.21 \pm 0.23 \text{ \%yr}^{-1}$). If a larger latitude region was
360 examined, these two model trend results will agree more poorly, although in our past experience,
361 the trend uncertainties do not get reduced nearly as much as a relationship following the inverse
362 of the square root of the number of bins. In Figure 4, MLS and CAM-chem-CEDS UT O_3 trend



363 sensitivity analysis is repeated for 2005–2018, 2005–2019, 2006–2020, and 2007–2020, showing
364 the relative insensitivity of the results to the choice of time period. Similar results are obtained
365 with WACCM (not shown).

366 For the UT CO trends, Figure 5 provides results in a similar way as shown in Fig. 3 for ozone,
367 but for just the two MLS CO retrieval levels at 147 and 215 hPa. In contrast to ozone, we can see
368 that the MLS-derived tropical UT CO values have typically decreased from 2005 to 2020; these
369 CO trends display negligible latitude dependence. Using the same approach as for ozone, but based
370 on the Fig. 5 results, we obtain an average MLS-based UT CO trend of $-0.25 \pm 0.30 \text{ \%yr}^{-1}$. The
371 trends at 215 hPa (-0.16 \%yr^{-1}) are a factor of two smaller than those at 147 hPa (-0.34 \%yr^{-1}),
372 although both of these numbers agree within the (2σ) trend uncertainties of 0.3 \%yr^{-1} . In contrast,
373 the average CAM-chem UT CO trend at these levels is $0.22 \pm 0.19 \text{ \% yr}^{-1}$, with little difference
374 between 147 and 215 hPa. The two models that use CEDS emissions (WACCM and CAM-chem-
375 CEDS) yield significantly smaller trends for CO, namely $0.0 \pm 0.14 \text{ \%yr}^{-1}$, with slightly negative
376 average trends at 147 hPa and slightly positive average trends at 215 hPa. However, there is not as
377 negative a tendency in the latter two model UT CO trends as in the MLS CO trends, especially if
378 one considers the aggregate values from different latitude bins; thus, there is some room for further
379 improvements in the modeled tropical CO UT trends, although the trends being compared have
380 fairly large error bars.

381 Furthermore, while the choice of time periods has some influence on UT CO trends, this choice
382 does not really alter the main conclusions provided above, as can be seen from Fig. 6, which is
383 analogous to the ozone trend sensitivity study provided in Fig. 4. Regarding another aspect of CO
384 trend sensitivities, we considered the issue of large peaks in the CO time series typically resulting
385 from El Niño related biomass burning events, followed by convective uplift and CO transport into
386 the UTLS. If the model has smaller peaks than the MLS data show, it may be that this could explain
387 some differences, or even a change of sign in the trends. This would stand out more if the large
388 peaks occurred close to the beginning or end of the time series. As a sensitivity test, we artificially
389 suppressed the peaks in these series by setting any CO value larger than 2.5 times the (1σ)
390 variability to a value of 1.5 times this variability, and we found the impact on the linear trends to
391 be negligible (well within the error bars shown here). Such a sensitivity study gives added
392 confidence in the robustness of these trends.



393 We illustrate the nature of some of the model and MLS tropical UT zonal mean time series in
394 the next two figures, which provide a view of the temporal variability in these series, as well as an
395 illustration of the MLR fits to the series. Figure 7 gives some time series examples for ozone at
396 12°N and 12°S at 147 and 215 hPa, with the MLS and model (WACCM) series and their respective
397 regression fits, along with the fitted trend lines. The linear correlation coefficients listed above
398 each panel provide a measure of how well the chemistry climate model can fit the MLS series
399 variability. These time series confirm the previously shown climatological mean differences
400 between WACCM and MLS ozone. The UT O₃ WACCM trends (dashed orange lines) roughly
401 follow the trends that are obtained from the MLS regression fits (dashed cyan lines), as expected
402 from the ozone trend summary plots (Fig. 3).

403 For CO, the time series provided in Fig. 8 show that there are some slight differences in the
404 trends between observed and modeled (WACCM) CO, with more negative trends in the MLS
405 series than in the model series, as shown earlier in the CO trend results of Fig. 6. The large
406 variability seen in the MLS CO series shows correlation with WACCM (see the large correlation
407 coefficient values, R , in the 12°S series for 147 and 215 hPa). We know that the largest CO peaks
408 in these time series are tied to surface emissions, convection, and subsequent transport into the
409 upper troposphere and lower stratosphere (UTLS), with a strong connection to El Niño-related
410 droughts and intense fire (biomass burning) events (see, e.g., Schoeberl et al., 2006, Jiang et al.,
411 2007, Liu et al., 2013, Park et al., 2021, Duncan et al., 2003, 2007). At 12°N, however, the
412 observed CO variability is somewhat smaller than at 12°S, and the model variability is much more
413 muted there, while the model versus MLS phase relationship is quite poor, especially at 215 hPa
414 (where R is negative, and the MLS time series annual phase is very poorly matched by the model).
415 We have checked that this poor correlation is not tied to an issue involving the smoothing of model
416 profiles to account for the MLS averaging kernels; indeed, Fig. S1 in the supplementary material
417 shows the small relative impact resulting from a smoothed (versus vertically interpolated) model
418 series on the average CO profile at 215 hPa and 12°N, as well as regarding the smoothed time
419 series and its phasing. In Fig. 9, we show the MLS and model (WACCM and CAM-chem-CEDS)
420 climatological mean CO changes over the annual cycle at 215 hPa for 12°N and 12°S, along with
421 the range of variability (twice the standard deviations about the means). The fits from the models
422 to the CO behavior at 12°S are quite good. These curves show the double peak structures
423 previously observed in seasonal analyses of biomass burning events, with related upward



424 injections of CO and their subsequent transport to the UT being implicated. Based on fire counts
425 from satellite data (see e.g., Duncan et al., 2003, 2007), the March biomass burning peaks have
426 been associated with the northern hemisphere (mainly from Southeast Asia, but also from northern
427 Africa), whereas the September/October peaks arise from the southern hemisphere (Indonesia,
428 Malaysia, Southern Africa, Brazil). We should also note (more broadly) that the climatological
429 double peak CO structure measured by MLS near 215 hPa over the broader (20°S–20 °N) tropics
430 is well matched by MIPAS CO zonal means (see SPARC DI, 2017, chapter 4). At 12°N, however,
431 the lack of correlation between the model variations and those deduced from MLS in Fig. 9 appears
432 to stem from the poorly modeled double peak structure; we also find that these poorer fits occur
433 more generally throughout the northern tropics. The model underestimates the boreal winter
434 buildup of CO (Gaubert et al., 2020; 2023), which may explain a poor representation of the
435 northern hemisphere March/April peak. Also, biomass burning emission biases can vary regionally
436 and this might explain some of the model/data differences, with some regions providing somewhat
437 better comparisons than others. We do not ascribe the larger model/MLS discrepancies at 215 hPa
438 in the northern tropics to an undue influence of the MLS a priori on the retrievals in this region, as
439 the (averaged) a priori MLS values (although not shown in Fig. 9) follow the WACCM model
440 fields quite well, and the MLS CO retrievals are producing significantly different variations. To
441 explore this hemispherical asymmetry further, we show CO column comparisons between zonal
442 mean time series from MOPITT, CAM-chem-CEDS and WACCM in Fig. 10; all CO columns are
443 averaged over the same latitudes (10°N–14°N and 10°S–14°S). The MOPITT values are obtained
444 from V9J (Deeter et al., 2022) Level 3 dry air total column data (X_{CO} in ppbv). Simulations are
445 smoothed by using the MOPITT a priori column as well as the 10 layers a priori and averaging
446 kernel profiles, as recommended for a quantitative comparison of modelled and MOPITT X_{CO} . We
447 obtain much better agreement in the phasing of these CO column comparisons for 12°N than we
448 do in the WACCM versus MLS CO comparisons at 215 hPa in Fig. 9, This is clearly seen in the
449 time series evolution, as well as in the correlation coefficients shown in both these Figures,
450 although R is slightly smaller at 12°N than at 12°S in Fig. 10 (but still about 0.75 to 0.8). We also
451 look at this issue for the gridded fields and provide R values for the 12°N and 12°S bins in Fig. 11,
452 where we superpose the column CO model results versus MOPITT and the 215 hPa model results
453 versus MLS as a function of longitude. Again, we observe that R is much higher for the CO total
454 columns than for the 215 hPa level, especially so in the northern tropics. The patterns versus



455 longitude indicate that poorer correlations exist over the Atlantic Ocean (just West of the
456 Greenwich meridian) than over land masses. We do not have clear explanations for the exact
457 patterns in Fig. 11, except for the suggestion that regions with strong land convection might show
458 better UT correlations between models and data, while outflow regions (downwind of convection)
459 in the upper troposphere could be more poorly modeled. Something (whether related to emissions,
460 convection, and/or transport) may be causing the models to not properly follow the observed UT
461 CO seasonal behavior in a narrow UT region of the northern tropics, even if the modeled seasonal
462 total columns compare well to MOPITT columns in that region; more in-depth analysis would be
463 needed to better probe these potential issues. Alternatively, it might be that currently unaccounted
464 for variations of the MLS vertical averaging kernels could affect the (properly smoothed) model
465 values in the northern hemisphere tropics at 215 hPa, in ways that are somehow significantly
466 different than what we show in Fig. S1; this is highly unlikely, given that the smoothed model
467 plots in this Figure hardly change if we replace the tropical MLS averaging kernel values used in
468 that plot by kernels appropriate for 70°N. Another potential issue might be poorly understood cloud
469 impacts on the 215 hPa MLS retrievals, specifically in the northern hemisphere tropics; although
470 this is speculative, it might be worth exploring in the future.

471 **3.3 Mapped trends**

472 We now turn to the mapped tropical UT trends by analyzing subsets of the O₃ and CO fields
473 from MLS and the models, based on monthly mean time series for 2005–2020 in latitude/longitude
474 bins, rather than on zonal means. As mentioned previously, these bins are also 4° wide in latitude,
475 and the longitude bins are 30° wide. The same regression methodology as described previously
476 here is used for each of the binned time series; we focus on the WACCM and CAM-chem-CEDS
477 ozone trends, as we have found that the CAM-chem and CAM-chem-CEDS results are quite
478 similar, in the case of ozone at least. Figure 12 shows the resulting mapped O₃ trends from MLS
479 and the two models for 147 and 215 hPa (top and bottom rows, respectively), with the maps
480 spanning 26°S to 26°N; hatched bins indicate a trend that is not statistically different from zero,
481 using 2σ bootstrap-derived uncertainties, as discussed above. The largest MLS trends are observed
482 over the Indonesian region and (mostly) to the East of that region, as well as over the Atlantic and
483 Africa; the Pacific region exhibits small trends, with a few of the bins showing a decreasing (but
484 non-significant) trend. The mapped trends confirm the overall zonal mean result of slightly larger



485 O₃ trends in MLS than in WACCM, and with an overall better/good agreement between the CAM
486 and MLS mapped O₃ trends. Broad regions with positive tendencies are observed in both model
487 trend results. Also, the error bars are large enough that the level of trend discrepancy is very rarely
488 statistically significant.

489 We have compared these mapped ozone trend results to those for tropospheric column ozone
490 (TCO) obtained by Ziemke et al. (2019), using a combination of total O₃ columns from the Aura
491 Ozone Monitoring Instrument (OMI) and MLS-based stratospheric O₃ columns. In Fig. 13, we
492 show in the top two rows the trends from MLS ozone at 178 hPa (top map) versus the bottom map
493 which provides the mapped TCO trends for the same time period, obtained from an appropriate
494 horizontal smoothing of the results obtained following the above reference, in order for the
495 resolutions to be comparable; this smoothing is simply obtained via interpolation versus latitude
496 and a weighted averaging in longitude, since the TCO results have significantly finer longitudinal
497 resolution (5°-wide bins) than the MLS longitudinal grid used here (30°-wide bins). Similarities
498 are observed in the longitudinal pattern of UT O₃ and TCO trends, as shown also for 3 different
499 latitude bins in panel (b) of Fig. 13; variations of a factor of two to three are observed between the
500 western and eastern hemispheres for both sets of trends, which tend to lie between roughly 0.3 and
501 1.2 % yr⁻¹. However, not all UT pressure levels and patterns of UT trends match the TCO trends
502 as well as shown here; this is seen from a set of correlation coefficient values provided in panel
503 (c), where different pressure levels for MLS-derived O₃ trends are used to indicate correlations
504 versus longitude as a function of latitude bin (on the y-axis). Indeed, one would not expect ozone
505 UT trend results to track TCO trends very well, given the sensitivity of the derived TCO trends,
506 which are affected more by the lower troposphere than the upper troposphere.

507 In Fig. 14, we show the mapped CO trend results for MLS and all three models (WACCM,
508 CAM-chem, and CAM-chem-CEDS) at 147 and 215 hPa. As seen above, MLS CO trends in the
509 UT are generally negative, with the more statistically significant result occurring at 147 hPa (where
510 the trends are more negative than at 215 hPa). There is an indication of slightly positive trends
511 over or near western Africa, mainly at 215 hPa, although this is not statistically significant. The
512 binned model results from CAM-chem confirm the zonal mean view from this model, with
513 generally near zero but often slightly positive trends, in disagreement with the MLS negative trend
514 results. When the CEDS emissions are used, as done for WACCM and CAM-chem-CEDS, there
515 is a general decrease in the UT CO trends, with some small negative values, although the vast



516 majority of the model CO trends obtained here are not statistically different from zero. Thus, the
517 use of CEDS emissions does result in a better agreement with the MLS negative UT CO trends,
518 but the MLS-derived trends are still more negative.

519 We have also analyzed the level of explained variance in the regression fits for these binned
520 trend results. Figure 15 shows the square of the correlation coefficient values (R^2) as a function of
521 latitude and longitude for different explanatory variables used in the binned O_3 fits at 147 hPa,
522 based on fit comparisons to the MLS series (top 6 panels), and for the regression fit versus the
523 WACCM series (bottom 6 panels). We have ignored the solar component in these plots as it was
524 found to be of negligible importance; we display the remaining contributions, namely the annual,
525 semi-annual, short-term (sum of the 3-month and 4-month terms), QBO, and ENSO terms, as well
526 as the contribution from the full regression fit, which shows that most (but certainly not all) of the
527 time series variance can be explained by such a regression model. The annual term and semi-
528 annual terms can generally explain a large part of the variance, usually followed in importance by
529 the ENSO term, at least over most of the Pacific. The QBO component is very small in the upper
530 troposphere, even though it is a well-known and large contributor to stratospheric trace gas
531 variability in the lowermost stratosphere, with a significant annual cycle in the tropical lowermost
532 stratosphere related to variations in vertical velocities and in the Brewer-Dobson circulation
533 (Randel et al., 2007; Witte et al., 2008). The R^2 patterns observed in the MLS panels are reproduced
534 in a broad sense by the fits to the CCM, as shown in the bottom 6 panels; this is also a result of the
535 close match between the CCM and the MLS O_3 time series, shown earlier in this work. However,
536 the ENSO model pattern for O_3 does not match the MLS-derived pattern that well over Indonesia,
537 and ENSO correlations in the CCM are often weaker than observed for the MLS ENSO R^2 ; this
538 comparison is generally better in the Pacific region between -90° and -180° . For the most part, it
539 does not matter much which model run is used for these analyses, or even which pressure level is
540 used; the results at 215 hPa (not shown) are quite similar to those in Fig. 15.

541 For CO, we repeat in Fig. 16 the explained variance analysis provided in Fig. 15 for O_3 . Overall,
542 the full fits explain less of the variability for CO, in part because of the large ENSO-related peaks
543 that occur throughout the MLS and WACCM records, which the regression model, as designed,
544 can only imperfectly match. Also, there are regions in the southern tropics where the annual cycle
545 in the model is better fit by the regression than in the MLS case, and this translates to a somewhat
546 better overall full fit. For both MLS and model, the semi-annual cycle component shows peaks



547 over the South Atlantic region, which is likely linked to biomass burning periods in this region and
548 related CO transport to the UT following convective activity (e.g., Duncan et al., 2007; Park et al.,
549 2013, 2021). The ENSO-related correlation patterns are broadly similar to the ozone case, for both
550 MLS and model representations. As for the ozone case, the QBO-related UT variability in the
551 tropics is very small (as seen from the QBO R^2 contributions).

552 To pursue the ENSO-related patterns further, one can obtain a (mapped) sensitivity coefficient
553 to ENSO from the regression fits regarding this component's importance in ppbv/K (where "K"
554 relates to tropical sea surface temperatures changes). The O_3 ENSO sensitivity is shown in Fig. 17
555 for the 2005–2020 MLS and WACCM results at 147 and 215 hPa. This provides more information
556 about the sign of the sensitivity over different regions, and we observe generally positive (negative)
557 sensitivity on the Eastern (Western) side of the maps, for both MLS and WACCM cases; moreover,
558 at least at 147 hPa, there are two strong negative minima on each side of the Equator in the central
559 Pacific region. The model results are quite consistent with those from MLS in terms of the ENSO-
560 related sensitivity coefficient patterns and magnitudes, although the model response is often
561 slightly smaller than seen in the MLS result. As we discuss further below, such ozone sensitivity
562 patterns have been described and interpreted before. Figure 18 provides the same analysis, but for
563 the CO sensitivity to ENSO. These maps show a positive CO ENSO sensitivity coefficient
564 throughout the tropics, with local maxima in both the Eastern and Western hemispheres, rather
565 than the O_3 dipole (positive/negative) structure shown in Fig. 17. The model CO ENSO sensitivity
566 broadly matches the MLS results, although it is not as strong; the different patterns in the western
567 hemisphere, compared to the O_3 sensitivity to ENSO, might be caused by differences in O_3 and
568 CO vertical profile gradients in these regions, but this would require further detailed investigations.
569 We also note that, especially in the MLS case, the peak magnitudes of the CO ENSO sensitivity
570 coefficients in Fig. 18 match the peak magnitudes of the positive O_3 ENSO sensitivity coefficients
571 in Fig. 17.

572 **4 Discussion and conclusions**

573 We have found some climatological differences between the MLS observations of O_3 and CO
574 in the tropical upper troposphere and WACCM6, as well as both CAM models considered here.
575 For O_3 , the models display a slight underestimate of the MLS values at 215 hPa; at 147 hPa (and
576 100 hPa), the models are biased high by at least 20%, and we have no reason to believe that positive



577 biases result from an average negative bias in the MLS UT values. For CO, the model
578 underestimates the MLS UT values by 10–20%, and in this case, these differences could be readily
579 caused by systematic biases in either MLS or the models, or both. Park et al. (2013) also found a
580 low model CO bias in a (WACCM4) simulation at 147 hPa, in comparison to ACE-FTS (and MLS)
581 data, especially in the SH sub-tropics; they attributed this to a possible underestimation of surface
582 emissions or transport via deep convection. We note that low biases in simulated tropospheric CO
583 have also been found before at northern latitudes and may arise from various factors, such as
584 underestimated CO emissions, high biases in modeled tropospheric OH (Strode et al., 2016;
585 Gaubert et al., 2023), or issues with simulated CO dry deposition rates (Stein et al., 2014). Based
586 on our model/MLS comparisons of UT CO seasonal changes, we find significantly poorer matches
587 at 215 hPa in the northern hemisphere tropics. The detailed causes of this discrepancy are currently
588 not clear to us, given the better matches (correlation coefficients) we obtain between MOPITT
589 total CO columns and modeled CO columns. Potential causes could include model inaccuracies
590 (possibly related to convection and/or CO emissions and subsequent transport in this fairly narrow
591 latitude region), or an alternate explanation having to do with poorly understood limitations of the
592 MLS data in this same region (see the previous section).

593 The variability that we have observed in the upper troposphere is difficult to fit completely
594 using standard linear regression, given the existence of short-term variability in the troposphere
595 (e.g., Dunkerton and Crum, 1995; Ziemke et al., 2015), as well as large episodic and somewhat
596 random enhancements in UT abundances (for CO in particular). Regarding this strong CO
597 variability, we note that ACE-FTS UT CO monthly zonal mean time series track those from MLS,
598 as shown by Park et al. (2021). The TCO interannual variability is also heavily influenced by
599 ENSO (Ziemke and Chandra, 2003; Ziemke et al., 2010). We found that the annual, semi-annual,
600 and ENSO terms dominate the ozone variability in the tropical upper troposphere. The MLS UT
601 ozone variations and their relation to ENSO, in particular, were discussed by Oman et al. (2013),
602 who showed patterns of ozone sensitivity to ENSO at 147 hPa (their Figure 6) that resemble the
603 ones we produced here (Fig. 16) from analyses of MLS data over almost twice as long a period.
604 Oman et al. (2013) also found that the ENSO relationship for ozone could be simulated by a
605 chemical climate model driven by observed SSTs. The observed and matching simulated
606 sensitivity coefficients imply increased downwelling from the stratosphere and suppressed
607 convection during El Niño periods for regions of positive sensitivity (Chandra et al., 1998; Sudo



608 and Takahashi, 2001; Oman et al., 2013). We find here that the CO sensitivity to ENSO is much
609 more spatially uniform in sign than the O₃ sensitivity; UT O₃ generally increases toward the
610 tropopause while CO decreases, leading to opposite sensitivities to increased upwelling phase
611 over the Pacific (Figs. 16 and 17). In some regions, the CO sensitivity has the same sign as for
612 ozone, and in other regions, it differs; moreover, the model's UT CO sensitivity coefficient to
613 ENSO seems to broadly match the observational sensitivity from MLS, as it shows positive values
614 throughout the tropics. These different behaviors between tropical UT O₃ and CO seem to mainly
615 reflect a stronger (and positive) sensitivity to biomass burning events in the case of CO.

616 Our multiple linear regression analyses lead to an averaged zonal mean tropical UT O₃ trend
617 from MLS for 2005–2020 of $0.39 \pm 0.28 \text{ \%yr}^{-1}$ (or about $0.22 \pm 0.16 \text{ ppbv yr}^{-1}$), where the error
618 bars indicate uncertainties at the 2σ level. We obtain excellent agreement with the above result
619 from CAM-chem-CEDS O₃ zonal mean trends ($0.38 \pm 0.28 \text{ \%yr}^{-1}$) and somewhat poorer
620 agreement from the smaller WACCM trends ($0.21 \pm 0.23 \text{ \%yr}^{-1}$). We also show that the zonal
621 mean O₃ tropical UT trend results for different time period choices, with start and end years
622 adjusted by one or two years, do not significantly depart from the 2005–2020 results. We note as
623 well that the MLS ozone profile trend detection capability lies within the most stable among ozone
624 sounders, based on the satellite and ground-based ozone intercomparison work by Hubert et al.
625 (2016). In addition, differences between stratospheric ozone columns from MLS and the Aura
626 Ozone Monitoring Instrument (OMI) exhibit no significant drift (Ziemke et al., 2019), thus
627 providing added confidence in the temporal stability of both measurement systems; we expect a
628 similar level of confidence in the stability of the MLS CO measurements, since CO is retrieved
629 using the same radiometer as the MLS standard ozone product. The largest MLS-derived mapped
630 O₃ trends (up to $+1.4\% \text{ yr}^{-1}$) are observed over Indonesia and East of that region, as well as over
631 the Atlantic and Africa; the Pacific region exhibits small or slightly negative trends. The mapped
632 MLS-based UT O₃ trends and TCO trends for the same period (see Fig. 13, based on the analyses
633 of Ziemke et al., 2019) provide good correlations in parts of the tropics, with similar values and
634 longitudinal patterns. In terms of the mapped model O₃ UT trends, they broadly match the MLS-
635 based UT trends, albeit with somewhat smaller variations. The Indonesian region displays much
636 smaller model O₃ trends than those derived from MLS data, and the western Pacific region exhibits
637 generally negative trends in the model, more so than in the MLS results.



638 The analyses by Wang et al. (2022) of the IAGOS commercial aircraft database for several
639 regions of the globe indicate that upper tropospheric O₃ values have increased from 1995–2017,
640 with some of the larger trends residing in the tropics. IAGOS-derived trends were previously
641 discussed by Cohen et al. (2018) for the 1994–2013 period, but with an emphasis on the extra-
642 tropics. The IAGOS trend analysis by Gaudel et al. (2020) for five tropical regions over 1994–
643 2016 gave positive UT trends in the range of 0.3–1.3 % yr⁻¹, with the largest values over Southeast
644 Asia and Malaysia/Indonesia. As mentioned above, the MLS results also show peak ozone trends
645 over this general region. The typical trends from Gaudel et al. (2020) are generally in accord with
646 (but somewhat larger than) the average tropical UT O₃ trends we obtain from the MLS data, which
647 provide more uniform (and daily) tropical coverage; we should note, however, that the time periods
648 are somewhat different for these rough comparisons, and this could account for some slowdown
649 in the more recent MLS O₃ trend results (compared to the 1994–2016 period). More detailed
650 comparisons between MLS and IAGOS are difficult and beyond the scope of this work, given the
651 differences in coverage (and in the vertical and horizontal footprints) between these measurement
652 systems; here, we therefore refer to fairly general past IAGOS-based results for both O₃ and CO.

653 There have been large differences between past satellite-based tropospheric O₃ trends (Gaudel
654 et al., 2018). Leventidou et al. (2018) pointed out that tropical tropospheric ozone column trends
655 derived from a combination of European satellite measurements from 1996 to 2015 showed
656 regional increases as large as 1–2%yr⁻¹, with some negative trends over the oceans, but with
657 significant uncertainties as well (see also Heue et al., 2016, and Ebojie et al., 2016). The TCO
658 analyses by Ziemke et al. (2019), using combined OMI and MLS ozone columns, showed that the
659 TCO trends are larger in the 2005–2016 time period than in the two decades before 2005; for the
660 former period, the TCO trends in the tropics are about 0.4–0.7 % yr⁻¹ (see also Gaudel et al., 2020);
661 there are regional TCO trend differences, with maxima over India, Southeast Asia and the Pacific
662 region slightly further East, as well as over the tropical Atlantic, with near zero or slightly negative
663 trends over the Western Pacific. Similar TCO trends (from OMI/MLS data) were also given by
664 Liu et al. (2022) for the slightly longer 2005–2018 period. Wang et al. (2022) showed that derived
665 ozone trends from ozonesonde profiles agree broadly with the IAGOS results, although the sonde
666 spatio-temporal coverage is naturally more limited, and there can be a fair amount of scatter in the
667 trends between different sonde sites. Thompson et al. (2021) observed significant seasonal
668 variations in derived tropical ozonesonde trends (based on data over the 1998–2019 period from



669 the Southern Hemisphere Additional Ozonesondes, or SHADOZ network); these authors noted
670 that dynamical influences (besides emissions changes) likely play a role in these tropical
671 tropospheric trends, which average 0.1–0.4 %yr⁻¹, but with trends in certain regions and seasons
672 (February to May in particular) as large as 1–2.5 %yr⁻¹.

673 Zhang et al. (2016) and Wang et al. (2022) have ascribed the positive sign of post-2000 tropical
674 ozone trends to an equatorward redistribution of surface emissions over the years. Moreover, Wang
675 et al. (2022) discussed how increases in aircraft emissions of nitrogen oxides should also have
676 contributed to enhancements in UT ozone. Most of the UT model O₃ trends shown in our work are
677 significantly (> 30–50%) larger in the NH tropics than in the SH tropics. This is also true for the
678 model simulation (also from CESM2) provided by Wang et al. (2022); these authors also point out
679 that uncertainties in estimates of ozone precursor emission inventories (including those for volatile
680 organic carbons species, or VOCs) may well contribute to differences between modeled and
681 observational ozone trends. We note that there are large differences (a range of a factor of two or
682 more) between the tropospheric ozone burden changes predicted by various global models in the
683 work by Wang et al. (2022). Liu et al. (2022) show that significant regional differences in ozone
684 column trends exist in their model results (using the NASA Goddard Earth Observing System
685 Chemistry Climate Model, GEOSCCM), with near zero trends over the tropical western Pacific;
686 their modeled TCO trend results underestimate the observed positive TCO trends. These authors
687 point to underestimates of ozone precursor emissions, notably for VOCs such as formaldehyde, as
688 a potential explanation for the model underestimates of some observed TCO increases (mostly in
689 the extra-tropics). While VOC source strengths might be difficult to invoke as a major source of
690 uncertainty for the tropical regions, other potential model issues (e.g., larger than currently
691 expected uncertainties in lightning-generated ozone in the tropical upper troposphere) may be
692 worth further consideration.

693 For the CO trends, the average tropical UT trend from MLS is -0.25 ± 0.30 %yr⁻¹, whereas the
694 corresponding trends from CAM-chem-CEDS and WACCM are near zero (0.0 ± 0.14 %yr⁻¹) for
695 this region. Therefore, there is room for improvements in the modeled tropical CO UT trends,
696 towards a better agreement versus the MLS-inferred results. We also note that the CAM-chem
697 simulations which use different inputs (not CEDS) for anthropogenic CO emissions (see Sect. 2),
698 yield positive average tropical UT CO trends ($+0.22 \pm 0.19$ %yr⁻¹) clearly not matching the MLS-
699 derived negative UT CO trends. As for the O₃ case, the zonal mean CO tropical UT trends for



700 slightly different time periods do not differ in a significant way from the 2005–2020 results. The
701 mapped MLS CO trends in the UT are also negative, with the more statistically significant result
702 (stronger negative trends) occurring at 147 hPa. While there have not been any past decades-long
703 trend estimates for CO in the broad tropical UT region, our results yield somewhat smaller rates
704 of decrease than other trends mentioned in the Introduction, for example -0.5 to -2 yr^{-1} , based on
705 IAGOS UT data at northern midlatitudes (Cohen et al., 2018). The mapped model UT CO trends
706 obtained here confirm the zonal mean model results. Although the CEDS emissions have helped
707 to produce near zero or slightly negative UT tropical CO trends in both WACCM and CAM-chem-
708 CEDS simulations, the MLS UT CO trends in the tropical UT are significantly more negative than
709 these model results. Column CO in the free troposphere has generally shown decreasing trends
710 since the turn of the century, typically between about -0.5 and -1.5 yr^{-1} , as observed in particular
711 by MOPITT and AIRS (Worden et al., 2013a, Strode et al., 2016; Buchholz et al., 2021; Hedelius
712 et al., 2021). Liu et al. (2022) presented a recent analysis of MOPITT CO data from 2005–2018,
713 along with tropospheric model comparisons to observed CO and O₃ time series. These authors
714 found (as shown here and described for MLS and ACE-FTS data by Park et al., 2021) that their
715 modeled and observational time series both exhibit large interannual variability, with some of the
716 largest interannual changes driven by El Niño events in 2006 and 2015 and related biomass burning
717 and CO enhancements tied to droughts over the Indonesian region (see also Logan et al., 2008;
718 Zhang et al., 2011; Livesey et al., 2013; Worden et al., 2013b; Park et al., 2013; Field et al., 2016).
719 Liu et al. (2022) found that modeled CO column trends over various regions of the globe were
720 generally negative, although a lower latitude region (India) exhibited a positive model trend. Jiang
721 et al. (2017) provide some arguments (and other references) pointing to flat biomass burning
722 emission trends over Africa for the first 10–15 years since the turn of the century. Not including
723 the strong tropical anomaly caused by El Niño in 2015, they infer a negative trend in global
724 biomass burning emissions. Uncertainties in the temporal evolution of OH (a major sink for CO)
725 could also explain model CO trend issues. However, Jiang et al. (2017) implied that uncertainties
726 in global OH would not readily explain global CO decreases, given constraints from methyl
727 chloroform surface data (this species also having OH as a major sink, as discussed as well by
728 Montzka et al., 2011). Rather, these authors conclude that decreasing CO emissions from
729 anthropogenic and biomass burning sources are the main cause of tropospheric CO decreases,
730 although some regional increasing emission trends do exist. While a systematic model bias cannot



731 readily lead to a significant discrepancy in model trend estimates (in percent per year) versus
732 observations, time-dependent emission biases could (e.g., Gaubert et al., 2023). To first order, the
733 decreasing UT CO tropical trends derived from MLS for 2005–2020 agree with (but tend to be
734 smaller in magnitude than) total column CO trends discussed previously in the literature. As
735 discussed by others, some non-linearity in CO trends may be responsible for some of the variability
736 in past tropospheric CO trend results.

737 We believe that further investigations into how well different models of O₃ and CO in the
738 tropical UT match the MLS UT trends in these species are warranted, to provide better
739 understanding of differences between models. There may still be adjustments to make to the
740 models regarding the assumed CO surface emissions, convection, and/or transport-related issues,
741 even though such detailed studies are beyond the scope of this paper. Indeed, biomass burning
742 from Africa or South America and emissions from Asia, followed by transport, can influence the
743 tropical upper tropospheric abundances of CO and O₃ (e.g., Tsvilidou et al., 2023). On a broader
744 note, the troposphere is a region where the relative importance of multiple factors might change
745 over the multi-decadal timescale of climate change; also, longer-term projections from (free
746 running) models may not be representative of changes from a particular decade or two (see Fiore
747 et al., 2022, regarding model ensemble projections). For example, while the MLS-derived ozone
748 trends in the tropical UT from 2005–2020 (a particular “snapshot” in time) compare fairly well
749 with other recent estimates of tropospheric ozone change over similar time periods, UT changes
750 may diverge from lower tropospheric changes in the longer-term. Long-term positive trends in the
751 influx of ozone from the stratosphere to the troposphere may be expected as a result of climate
752 change (Meul et al., 2018), probably with more of a significant influence on the extra-tropical
753 upper troposphere. Regarding the tropics, Stevenson et al. (2013) showed that a number of
754 chemistry climate model simulations of climate change scenarios yielded long-term ozone
755 decreases in the lower troposphere as a result of enhancements in water vapor (implying more
756 ozone destruction), but low latitude upper tropospheric ozone could be expected to rise, following
757 increased production from lightning. Finally, obtaining accurate enough observations of large-
758 scale tropospheric composition change over the long-term is expected to represent a continuing,
759 but worthy challenge.

760

761



762 **Data availability.**

763 The MLS data files analyzed here come from the MLS Level 3 data sets (zonal mean and gridded
764 quantities), which are publicly available from the Goddard Earth Sciences Data and Information Services
765 Center (GES DISC) at <https://earthdata.nasa.gov/eosdis/daacs/gesdisc>.
766 The MOPITT Version 9 products are available from NASA through the Earthdata portal
767 (<https://earthdata.nasa.gov/>; https://asdc.larc.nasa.gov/project/MOPITT/MOP03JM_9; or directly from the
768 ASDC archive (<https://asdc.larc.nasa.gov/data/MOPITT/>). We used the following site,
769 ftp://ftp.seismo.nrcan.gc.ca/spaceweather/solar_flux/monthly_averages/solflux_monthly_average.txt to
770 obtain monthly means of the Canadian F10.7 solar flux measurements (Tapping, 2013); these series (see
771 <http://www.spaceweather.gc.ca>) were included in our regression fits. The QBO-related equatorial wind
772 monthly time series were obtained from the public website at [https://www.geo.fu-](https://www.geo.fu-berlin.de/en/met/ag/strat/produkte/qbo)
773 [berlin.de/en/met/ag/strat/produkte/qbo](https://www.geo.fu-berlin.de/en/met/ag/strat/produkte/qbo). The multivariate ENSO index dataset was obtained from the NOAA
774 Physical Sciences Laboratory website at <https://www.psl.noaa.gov/enso/mei/> (Wolter and Timlin, 2011;
775 Zhang et al., 2019). OMI/MLS tropospheric ozone data were obtained from the NASA satellite tropospheric
776 ozone webpage https://acd-ext.gsfc.nasa.gov/Data_services/cloud_slice/.

777

778 **Supplement.** Additional short supplementary material is included in this submission as a separate file.

779

780 **Author contributions.** LF analyzed the MLS and model data for trends and variability, and prepared the
781 manuscript, along with contributions from all co-authors. DEK, CGB, and BCG provided inputs for running
782 the model runs, as well as properly averaged and formatted outputs from the model, as well as pertinent
783 model-related comments and interpretation of results. JRZ provided TCO datasets and comments on the
784 manuscript. NJL, MJS, WGR, and others on the MLS team provided analyses and expertise to enable the
785 production of the Aura MLS data sets; NJL, MJS, and WGR also provided comments on the manuscript;
786 RAF provided programming assistance for the creation of the MLS data sets and for storage and analyses
787 of the MLS and model files.

788

789 **Competing interests.** The authors declare that they have no conflict of interest.

790

791 **Acknowledgments.** We are thankful to the whole MLS team (past and present) for their contributions over
792 the years to the MLS instrument, data, processing, and database management. WACCM is a component of
793 the CESM, supported by the National Science Foundation (NSF). We acknowledge high-performance
794 computing support from Cheyenne (doi:10.5065/D6RX99HX) provided by NCAR's Computational and
795 Information Systems Laboratory, sponsored by the NSF. F10.7 data collection and dissemination are



796 supported by the National Research Council of Canada, with the participation of Natural Resources Canada
797 and support by the Canadian Space Agency. Work at the Jet Propulsion Laboratory, California Institute of
798 Technology, was performed under contract with the National Aeronautics and Space Administration
799 (80NM0018D0004). Copyright 2024. All rights reserved.

800

801 **Financial support.** LF and RAF were funded by the NASA Atmospheric Composition Modeling and
802 Analysis Program (ACMAP). NJL, MJS, and WGR (as well as LF) were supported by the Aura Microwave
803 Limb Sounder project. DEK, BG, and CGB were funded separately by NASA and NSF grants. Part of this
804 material is based on work supported by the National Center for Atmospheric Research, which is a major
805 facility sponsored by the National Science Foundation under Cooperative Agreement No. 1852977. The
806 NSF NCAR MOPITT project is supported by the National Aeronautics and Space Administration (NASA)
807 Earth Observing System (EOS) program.



808 References

- 809 Bouarar, I., Gaubert, B., Brasseur, G. P., Steinbrecht, W., Doumbia, T., Tilmes, S., et al.: Ozone anomalies in the free
810 troposphere during the COVID-19 pandemic, *Geophys. Res. Lett.*, 48, e2021GL094204.
811 <https://doi.org/10.1029/2021GL094204>, 2021.
- 812 Bourassa, A. E., Degenstein, D. A., Randel, W. J., Zawodny, J. M., Kyrölä, E., McLinden, C. A., Sioris, C. E., and
813 Roth, C. Z.: Trends in stratospheric ozone derived from merged SAGE II and Odin-OSIRIS satellite observations,
814 *Atmos. Chem. Phys.*, 14, 6983-6994, <https://doi.org/10.5194/acp-14-6983-2014>, 2014.
- 815 Buchholz, B. R., Worden H. M., et al.: Air pollution trends measured from Terra: CO and AOD over industrial, fire-
816 prone, and background regions, *Remote Sensing of Environment*, 256, 112275,
817 <https://doi.org/10.1016/j.rse.2020.112275>, 2021.
- 818 Burkholder, J. B., Sander, S. P., Abbatt, J. P. D., Barker, J. R., Cappa, C., Crounse, J. D., Dibble, T. S., Huie, R. E.,
819 Kolb, C. E., Kurylo, M. J., Orkin, V. L., Percival, C. J., Wilmouth, D. M., and Wine, P. H.: Chemical kinetics and
820 photochemical data for use in atmospheric studies, Evaluation No. 19, JPL Publication 19-5, Jet Propulsion
821 Laboratory, California Institute of Technology, Pasadena, <http://jpldataeval.jpl.nasa.gov> (last access: 1 March
822 2022), 2019.
- 823 Calvo, N., Garcia, R. R., Randel, W. J., and Marsh, D.: Dynamical mechanism for the increase in tropical upwelling
824 in the lowermost tropical stratosphere during warm ENSO events, *J. Atmos. Sci.*, 67, 2331–2340,
825 <https://doi.org/10.1175/2010JAS3433.1>, 2010.
- 826 Chandra, S., Ziemke, J. R., Min, W., and Read, W. G.: Effects of 1997–1998 El Niño on tropospheric ozone and water
827 vapor, *Geophys. Res. Lett.*, 25(20), 3867–3870, <https://doi.org/10.1029/98GL02695>, 1998.
- 828 Coddington, O., Lean, J., Pilewskie, P., Snow, M., and Lindholm, D.: A solar irradiance climate data record, *Bull.*
829 *Amer. Meteor. Soc.*, <https://doi.org/10.1175/BAMS-D-14-00265.1>, 2016.
- 830 Cohen, Y., Petetin, H., Thouret, V., Marécal, V., Josse, B., Clark, H., Sauvage, B., Fontaine, A., Athier, G., Blot, R.,
831 Boulanger, D., Cousin, J.-M., and Nédélec, P.: Climatology and long-term evolution of ozone and carbon
832 monoxide in the upper troposphere–lower stratosphere (UTLS) at northern midlatitudes, as seen by IAGOS from
833 1995 to 2013, *Atmos. Chem. Phys.*, 18, 5415–5453, <https://doi.org/10.5194/acp-18-5415-2018>, 2018.
- 834 Collins, W. J., Derwent, R. G., Garnier, B., C. E. Johnson, C. E., Sanderson, M. G., and Stevenson, D. S.: Effect of
835 stratosphere-troposphere exchange on the future tropospheric ozone trend, *J. Geophys. Res.*, 108, D12, 8528,
836 <https://doi.org/10.1029/2002JD002617>, 2003.
- 837 Cooper, O. R., Parrish, D. D., Ziemke, J. R., Balashov, N. V., Cupeiro, M., Galbally, I., Gilge, S., Horowitz, L., Jensen,
838 N. R., Lamarque, J.-F., Naik, V., Oltmans, S. J., Schwab, J., Shindell, D. T., Thompson, A. M., Thouret, V., Wang,
839 Y., and Zbinden, R. M.: Global distribution and trends of tropospheric ozone: An observation-based review,
840 *Elementa*, 2, 000029, <https://doi.org/10.12952/journal.elementa.000029>, 2014.
- 841 Crutzen, P. J.: A discussion of the chemistry of some minor constituents in stratosphere and troposphere, *Pure Appl.*
842 *Geophys.*, 106, 1385–1399, <https://doi.org/10.1007/BF00881092>, 1973.
- 843 Crutzen, P. J., and Andreae, M. O.: Biomass burning in the tropics: Impact on atmospheric chemistry and
844 biogeochemical cycles, *Science*, 250, 1669–1678, <https://doi.org/10.1126/science.250.4988.1669>, 1990.



- 845 Danabasoglu, G., Lamarque, J.-F., Bacmeister, J., Bailey, D. A., DuVivier, A. K., Edwards, J., Emmons, L. K.,
846 Fasullo, J., Garcia, R., Gettelman, A., Hannay, C., Holland, M. M., Large, W. G., Lauritzen, P. H., Lawrence, D.
847 M., Lenaerts, J. T. M., Lindsay, K., Lipscomb, W. H., Mills, M. J., Neale, R., Oleson, K. W., Otto-Bliesner, B.,
848 Phillips, A. S., Sacks, W., Tilmes, S., van Kampenhout, L., Vertenstein, M., Bertini, A., Dennis, J., Deser, C.,
849 Fischer, C., Fox-Kemper, B., Kay, J. E., Kinnison, D. E., Kushner, P. J., Larson, V. E., Long, M. C.,
850 Mickelson, S., Moore, J. K., Nienhouse, E., Polvani, L., Rasch, P. J., and Strand, W. G.: The Community Earth
851 System Model Version 2 (CESM2), *J. Adv. in Modeling Earth Systems*, 12,
852 <https://doi.org/10.1029/2019MS001916>, 2020.
- 853 Darmenov, A., and da Silva, A. M.: The Quick Fire Emissions Dataset (QFED) - Documentation of versions 2.1, 2.2
854 and 2.4, NASA/TM–2015–104606, 2015;38:183, <http://gmao.gsfc.nasa.gov/pubs/tm/>, 2014.
- 855 Davis, N. A., Callaghan, P., Simpson, I. R., and Tilmes, S.: Specified dynamics scheme impacts on wave-mean flow
856 dynamics, convection, and tracer transport in CESM2 (WACCM6), *Atmos. Chem. Phys.*, 22, 197–
857 214, <https://doi.org/10.5194/acp-22-197-2022>, 2022.
- 858 Deeter, M., Francis, G., Gille, J., Mao, D., Martínez-Alonso, S., Worden, H., Ziskin, D., Drummond, J., Commane,
859 R., Diskin, G., and McKain, K.: The MOPITT Version 9 CO product: sampling enhancements and validation,
860 *Atmos. Meas. Tech.*, 15, 2325–2344, <https://doi.org/10.5194/amt-15-2325-2022>, 2022.
- 861 Doherty, R. M., Stevenson, D. S., Johnson, C. E., Collins, W. J., and Sanderson, M. G.: Tropospheric ozone and El
862 Niño–Southern Oscillation: Influence of atmospheric dynamics, biomass burning emissions, and future climate
863 change, *J. Geophys. Res.-Atmos.*, 111, D19304, <https://doi.org/10.1029/2005JD006849>, 2006.
- 864 Duncan, B. N., Martin, R. V., Staudt, A. C., Yevich, R., and Logan, J. A.: Interannual and seasonal variability of
865 biomass burning emissions constrained by satellite observations, *J. Geophys. Res.-Atmos.*, 108, 4100,
866 <https://doi.org/10.1029/2002jd002378>, 2003.
- 867 Duncan, B. N., Strahan, S. E., Yoshida, Y., Steenrod, S. D., and Livesey, N.: Model study of the cross-tropopause
868 transport of biomass burning pollution, *Atmos. Chem. Phys.*, 7, 3713–3736, [https://doi.org/10.5194/acp-7-3713-](https://doi.org/10.5194/acp-7-3713-2007)
869 [2007](https://doi.org/10.5194/acp-7-3713-2007), 2007.
- 870 Dunkerton, T. J., and Crum, F. X.: Eastward propagating eastward ~2- to 15-day equatorial convection and its relation
871 to the tropical intraseasonal oscillation, *J. Geophys. Res.*, 100, D12, 25781–25790,
872 <http://dx.doi.org/10.1029/95JD02678>, 1995.
- 873 Ebojje, F., Burrows, J. P., Gebhardt, C., Ladstetter-Weienmayer, A., von Savigny, C., Rozanov, A., Weber, M., and
874 Bovensmann, H.: Global tropospheric ozone variations from 2003 to 2011 as seen by SCIAMACHY, *Atmos.*
875 *Chem. Phys.*, 16, 417–436, <https://doi.org/10.5194/acp-16-417-2016>, 2016.
- 876 Efron, B., and Tibshirani, R.: *An Introduction to the Bootstrap*, Monographs on Statistics and Applied Probability 57,
877 Chapman and Hall, 1993.
- 878 Emmons, L. K., Schwantes, R. H., Orlando, J. J., Tyndall, G., Kinnison, D., Lamarque, J.-F., Marsh, D., Mills, M. J.,
879 Tilmes, S., Bardeen, C., Buchholz, R. R., Conley, A., Gettelman, A., Garcia, R., Simpson, I., Blake, D. R.,
880 Meinardi, S., and Pétron, G.: The Chemistry Mechanism in the Community Earth System Model version 2
881 (CESM2), *Journal of Advances in Modeling Earth Systems*, 12, <https://doi.org/10.1029/2019MS001882>, 2020.



- 882 Feely, R. A., Gammon, R. H., Taft, B. A., Pullen, P. E., Waterman, L. S., Conway, T. J., Gendron, J. F., and
883 Wisegarver, D. P.: Distribution of chemical tracers in the eastern equatorial Pacific during and after the 1982–
884 1983 El Niño/Southern Oscillation Event, *J. Geophys. Res.-Oceans*, 92, 6545–6558,
885 <https://doi.org/10.1029/JC092iC06p06545>, 1987.
- 886 Field, R. D., van der Werf, G. R., Fanin, T., Fetzer, E. J., Fuller, R., Jethva, H., Levy, R., Livesey, N. J., Luo, M.,
887 Torres, O., and Worden, H. M.: Indonesian fire activity and smoke pollution in 2015 show persistent nonlinear
888 sensitivity to El Niño-induced drought, *Proceedings of the National Academy of Sciences of the United States of*
889 *America*, 113, 9204–9209, <https://doi.org/10.1073/pnas.1524888113>, 2016.
- 890 Fiore, A. M., Hancock, S. E., Lamarque, J.-F., Correa, G. P., Chang, K.-L., Ru, M., Cooper, O., Gaudel, A., Polvani,
891 L. M., Sauvage, B., and Ziemke, J. R.: Understanding recent tropospheric ozone trends in the context of large
892 internal variability: a new perspective from chemistry-climate model ensembles, *Environ. Res.: Climate* 1 (2022)
893 025008, <https://doi.org/10.1088/2752-5295/ac9cc2>, 2022.
- 894 Froidevaux, L., Kinnison, D. E., Wang, R., Anderson, J., and Fuller, R. A.: Evaluation of CESM1 (WACCM) free-
895 running and specified dynamics atmospheric composition simulations using global multispecies satellite data
896 records, *Atmos. Chem. Phys.*, 19, 4783–4821, <https://doi.org/10.5194/acp-19-4783-2019>, 2019.
- 897 Froidevaux, L., Kinnison, D. E., Santee, M. L., Millán, L. F., Livesey, N. J., Read, W. G., Bardeen, C. G., Orlando, J.
898 J., and Fuller, R. A.: Upper stratospheric ClO and HOCl trends (2005–2020): Aura Microwave Limb Sounder and
899 model results, *Atmos. Chem. Phys.*, 22, 4779–4799, <https://doi.org/10.5194/acp-22-4779-2022>, 2022.
- 900 Gaubert, B., Worden, H. M., Arellano, A. F. J., Emmons, L. K., Tilmes, S., Barré, J., Martínez Alonso, S., Vitt, F.,
901 Anderson, J. L., Alkemade, F., Houweling, S., and Edwards, D. P.: Chemical feedback from decreasing carbon
902 monoxide emissions, *Geophys. Res. Lett.*, 44, 9985–9995, <https://doi.org/10.1002/2017GL074987>, 2017.
- 903 Gaubert, B., Emmons, L. K., Raeder, K., Tilmes, S., Miyazaki, K., Arellano Jr., A. F., Elguindi, N., Granier, C., Tang,
904 W., Barré, J., Worden, H. M., Buchholz, R. R., Edwards, D. P., Franke, P., Anderson, J. L., Saunio, M., Schroeder,
905 J., Woo, J.-H., Simpson, I. J., Blake, D. R., Meinardi, S., Wennberg, P. O., Crouse, J., Teng, A., Kim, M.,
906 Dickerson, R. R., He, H., Ren, X., Pusede, S. E., and Diskin, G. S.: Correcting model biases of CO in East Asia:
907 impact on oxidant distributions during KORUS-AQ, *Atmos. Chem. Phys.*, 20, 14617–14647,
908 <https://doi.org/10.5194/acp-20-14617-2020>, 2020.
- 909 Gaubert, B., Edwards, D. P., Anderson, J. L., Arellano, A.F., Barré, J., Buchholz, R.R., Darras, S., Emmons, L.K.,
910 Fillmore, D., Granier, C., et al.: Global Scale Inversions from MOPITT CO and MODIS AOD, *Remote Sens.* 15,
911 4813, <https://doi.org/10.3390/rs15194813>, 2023.
- 912 Gaudel, A., Cooper, O. R., Ancellet, G., Barret, B., Boynard, A., Burrows, J. P., Clerbaux, C., Coheur, P. F., Cuesta,
913 J., Cuevas, E., Doniki, S., Dufour, G., Ebojje, F., Foret, G., Garcia, O., Granados-Muñoz, M. J., Hannigan, J. W.,
914 Hase, F., Hassler, B., Huang, G., Hurtmans, D., Jaffe, D., Jones, N., Kalabokas, P., Kerridge, B., Kulawik, S.,
915 Latter, B., Leblanc, T., Le Flochmoën, E., Lin, W., Liu, J., Liu, X., Mahieu, E., McClure-Begley, A., Neu, J. L.,
916 Osman, M., Palm, M., Petetin, H., Petropavlovskikh, I., Querel, R., Rahpoe, N., Rozanov, A., Schultz, M. G.,
917 Schwab, J., Siddans, R., Smale, D., Steinbacher, M., Tanimoto, H., Tarasick, D. W., Thouret, V., Thompson, A.
918 M., Trickl, T., Weatherhead, E., Wespes, C., Worden, H. M., Vigouroux, C., Xu, X., Zeng, G., and Ziemke, J.:



- 919 Tropospheric Ozone Assessment Report: Present-day distribution and trends of tropospheric ozone relevant to
920 climate and global atmospheric chemistry model evaluation, *Elem. Sci. Anth.*, 6, 39,
921 <https://doi.org/10.1525/elementa.291>, 2018.
- 922 Gaudel, A., Cooper, O. R., Chang, K.-L., Bourgeois, I., Ziemke, J. R., Strode, S. A., Oman, L. D., Sellitto, P., Nédélec,
923 P., Blot, R., Thouret, V., and Granier, C.: Aircraft observations since the 1990s reveal increases of tropospheric
924 ozone at multiple locations across the Northern Hemisphere, *Sci. Adv.*, 6, eaba8272,
925 <https://doi.org/10.1126/sciadv.aba8272>, 2020.
- 926 Gelaro, R., McCarty, W., Suarez, M. J., Todling, R., Molod, A., Takacs, L., Randles, C. A., Darmenov,
927 A., Bosilovich, M. G., Reichle, R., Wargan, K., Coy, L., Cullather, R., Draper, C., Akella, S., Buchard,
928 V., Conaty, A., da Silva, A. M., Gu, W., Kim, G.-K., Koster, R., Lucchesi, R., Merkova, D., Nielsen, J.
929 E., Partyka, G., Pawson, S., Putman, W., Rienecker, M., Schubert, S. D., Sienkiewicz, M., and Zhao, B.: The
930 Modern-Era Retrospective Analysis for Research and Applications, Version 2 (MERRA2), *J. Clim.*, 30, 5419–
931 5454, <https://doi.org/10.1175/JCLI-D-16-0758.1>, 2017.
- 932 Gettelman, A., Mills, M. J., Kinnison, D. E., Garcia, R. R., Smith, A. K., Marsh, D. R., Tilmes, S., Vitt, F., Bardeen,
933 C. G., McInerney, J., Liu, H.-L., Solomon, S. C., Polvani, L. M., Emmons, L. K., Lamarque, J.-F., Richter, J. H.,
934 Glanville, A. S., Bacmeister, J. T., Phillips, A. S., Neale, R. B., Simpson, I. R., DuVivier, A. K., Hodzic, A., and
935 Randel, W. J.: The Whole Atmosphere Community Climate Model version 6 (WACCM6), *J. Geophys. Res.-*
936 *Atmos.*, 124, 12,380–12,403, <https://doi.org/10.1029/2019JD030943>, 2019.
- 937 Gratz, L. E., Jaffe, D. A., and Hee, J. R.: Causes of increasing ozone and decreasing carbon monoxide in springtime
938 at the Mt. Bachelor Observatory from 2004 to 2013, *Atm. Env.*, 109, 323–330,
939 <http://dx.doi.org/10.1016/j.atmosenv.2014.05.076>, 2015.
- 940 He, H., Stehr, J. W., Hains, J. C., Krask, D. J., Doddridge, B. G., Vinnikov, K. Y., Canty, T. P., Hosley, K. M.,
941 Salawitch, R. J., Worden, H. M., and Dickerson, R. R.: Trends in emissions and concentrations of air pollutants in
942 the lower troposphere in the Baltimore/Washington airshed from 1997 to 2011, *Atmos. Chem. Phys.* 13,
943 <https://doi.org/10.5194/acp-13-7859-2013>, 2013.
- 944 Hedelius, J. K., Toon, G. C., Buchholz, R. R., Iraci, L. T., Podolske, J. R., Roehl, C. M., et al.: Regional and urban
945 column CO trends and anomalies as observed by MOPITT over 16 years, *J. Geophys. Res.-Atmos.*, 126,
946 e2020JD033967, <https://doi.org/10.1029/2020JD033967>, 2021.
- 947 Hegglin, M. I., and Shepherd, T. G.: Large Climate-Induced Changes in Ultraviolet Index and Stratosphere-to
948 Troposphere Ozone Flux, *Nature Geoscience*, 2, 687–691, <http://dx.doi.org/10.1038/ngeo604>, 2009.
- 949 Hegglin, M. I., Tegtmeier, S., Anderson, J., Bourassa, A. E., Brohede, S., Degenstein, D., Froidevaux, L., Funke, B.,
950 Gille, J., Kasai, Y., Kyrölä, E. T., Lumpe, J., Murtagh, D., Neu, J. L., Pérot, K., Remsberg, E. E., Rozanov, A.,
951 Toohey, M., Urban, J., von Clarmann, T., Walker, K. A., Wang, H.-J., Arosio, C., Damadeo, R., Fuller, R. A.,
952 Lingenfelter, G., McLinden, C., Pendlebury, D., Roth, C., Ryan, N. J., Sioris, C., Smith, L., and Weigel, K.:
953 Overview and update of the SPARC Data Initiative: comparison of stratospheric composition measurements from
954 satellite limb sounders, *Earth Syst. Sci. Data*, 13, 1855–1903, <https://10.5194/essd-13-1855-2021>, 2021.



- 955 Hess, P. G., and Zbinden, R.: Stratospheric impact on tropospheric ozone variability and trends: 1990–2009, *Atmos.*
956 *Chem. Phys.*, 13, 649–674, <https://doi.org/10.5194/acp-13-649-2013>, 2013.
- 957 Heue, K.-P., Coldewey-Egbers, M., Delcloo, A., Lerot, C., Loyola, D., Valks, P., and van Roozendael, M.: *Atmos.*
958 *Meas. Tech.*, 9, 5037–5051, <https://doi.org/10.5194/amt-9-5037-2016>, 2016.
- 959 Hsu, J. and Prather, M. J.: Is the residual vertical velocity a good proxy for stratosphere-troposphere exchange of
960 ozone?, *Geophys. Res. Lett.*, 41, 9024–9032, <https://doi.org/10.1002/2014GL061994>, 2014.
- 961 Huang, L., Fu, R., Jiang, J. H., Wright, J. S., and Luo, M.: Geographic and seasonal distributions of CO transport
962 pathways and their roles in determining CO centers in the upper troposphere, *Atmos. Chem. Phys.*, 12, 4683–4698,
963 <https://doi.org/10.5194/acp-12-4683-2012>, 2012.
- 964 Huang, L., Fu, R., and Jiang, J. H.: Impacts of fire emissions and transport pathways on the interannual variation of
965 CO in the tropical upper troposphere, *Atmos. Chem. Phys.*, 14, 4087–4099, [https://doi.org/10.5194/acp-14-4087-](https://doi.org/10.5194/acp-14-4087-2014)
966 [2014](https://doi.org/10.5194/acp-14-4087-2014), 2014.
- 967 Huang, L., Jiang, J. H., Murray, L. T., Damon, M. R., Su, H., and Livesey, N. J.: Evaluation of UTLS carbon monoxide
968 simulations in GMI and GEOS-Chem chemical transport models using Aura MLS observations, *Atmos. Chem.*
969 *Phys.*, 16, 5641–5663, <https://doi.org/10.5194/acp-16-5641-2016>, 2016.
- 970 Hubert, D., Lambert, J.-C., Verhoelst, T., Granville, J., Keppens, A., Baray, J.-L., Bourassa, A. E., Cortesi, U.,
971 Degenstein, D. A., Froidevaux, L., Godin-Beekmann, S., Hoppel, K. W., Johnson, B. J., Kyrölä, E., Leblanc, T.,
972 Lichtenberg, G., Marchand, M., McElroy, C. T., Murtagh, D., Nakane, H., Portafaix, T., Querel, R., Russell III, J.
973 M., Salvador, J., Smit, H. G. J., Stebel, K., Steinbrecht, W., Strawbridge, K. B., Stübi, R., Swart, D. P. J., Taha,
974 G., Tarasick, D. W., Thompson, A. M., Urban, J., van Gijssel, J. A. E., Van Malderen, R., von der Gathen, P.,
975 Walker, K. A., Wolfram, E., and Zawodny, J. M.: Ground-based assessment of the bias and long-term stability of
976 14 limb and occultation ozone profile data records, *Atmos. Meas. Tech.*, 9, 2497–2534,
977 <https://doi.org/10.5194/amt-9-2497-2016>, 2016.
- 978 Jiang, J. H., Livesey, N. J., Su, H., Neary, L., McConnell, J. C., and Richards, N. A. D.: Connecting surface emissions,
979 convective uplifting, and long-range transport of carbon monoxide in the upper troposphere: New observations
980 from the Aura Microwave Limb Sounder, *Geophys. Res. Lett.*, 34, L18812, <https://doi.org/10.1029/2007gl030638>,
981 2007.
- 982 Jiang, Z., Worden, J. R., Worden, H., Deeter, M., Jones, D. B. A., Arellano, A. F., and Henze, D. K.: A 15-year record
983 of CO emissions constrained by MOPITT CO observations, *Atmos. Chem. Phys.*, 17, 4565–4583,
984 <https://doi.org/10.5194/acp17-4565-2017>, 2017.
- 985 Jones, C. D., Collins, M., Cox, P. M., and Spall, S. A.: The Carbon Cycle Response to ENSO: A Coupled Climate–
986 Carbon Cycle Model Study, *J. Climate*, 14, 4113–4129, [https://doi.org/10.1175/1520-](https://doi.org/10.1175/1520-0442(2001)014<4113:tccte>2.0.CO;2)
987 [0442\(2001\)014<4113:tccte>2.0.CO;2](https://doi.org/10.1175/1520-0442(2001)014<4113:tccte>2.0.CO;2), 2001.
- 988 Kinnison, D. E., Brasseur, G. P., Walters, S., Garcia, R. R., Sassi, F., Boville, B. A., Marsh, D. Harvey, L., Randall,
989 C., Randel, W., Lamarque, J. F., Emmons, L. K., Hess, Orlando, J., Tyndall, G., and Pan, L.: Sensitivity of
990 chemical tracers to meteorological parameters in the MOZART-3 chemical transport model, *J. Geophys. Res.*,
991 112, D20302, <https://doi.org/10.1029/2006JD007879>, 2007.



- 992 Khalil, M. A. K., and Rasmussen, R. A.: The global cycle of carbon monoxide: trends and mass balance, *Chemosphere*,
993 20, Nos. 1–2, pp. 227–242, [https://doi.org/10.1016/0045-6535\(90\)90098-E](https://doi.org/10.1016/0045-6535(90)90098-E), 1990.
- 994 Kumar, A., Wu, S., Weise, M. F., Honrath, R., Owen, R. C., Helmig, D., Kramer, L., Val Martin, M., and Li, Q.: Free-
995 troposphere ozone and carbon monoxide over the North Atlantic for 2001–2011, *Atmos. Chem. Phys.*, 13, 12537–
996 12547, <https://doi.org/10.5194/acp-13-12537-2013>, 2013.
- 997 Laken, B. A., and Shahbaz, T.: Satellite-Detected Carbon Monoxide Pollution during 2000–2012: Examining Global
998 Trends and also Regional Anthropogenic Periods over China, the EU and the USA, *Climate*, 2014, 2, 1-16,
999 <https://doi.org/10.3390/cli2010001>, 2014.
- 1000 Leventidou, E., Weber, M., Eichmann, K.-U., Burrows, J. P., Heue, K.-P., Thompson, A. M., and Johnson, B. J.:
1001 Harmonisation and trends of 20-year tropical tropospheric ozone data, *Atmos. Chem. Phys.*, 18, 9189–9205,
1002 <https://doi.org/10.5194/acp-18-9189-2018>, 2018.
- 1003 Li, L., and Liu, Y.: Space-borne and ground observations of the characteristics of CO pollution in Beijing, 2000–2010,
1004 *Atmos. Env.*, 45, 2367–2372. <https://doi.org/10.1016/j.atmosenv.2011.02.026>, 2011.
- 1005 Liu, J., Logan, J. A., Murray, L. T., Pumphrey, H. C., Schwartz, M. J., and Megretskaja, I. A.: Transport analysis and
1006 source attribution of seasonal and interannual variability of CO in the tropical upper troposphere and lower
1007 stratosphere, *Atmos. Chem. Physics*, 13, 129–146. <https://doi.org/10.5194/acp-13-129-2013>, 2013.
- 1008 Liu, J., Strode, S. A., Liang, Q., Oman, L. D., Colarco, P. R., Fleming, E. L., Manyin, M. E., Douglass, A. R., Ziemke,
1009 J. R., Lamsal, L. N., and Li, C.: Change in tropospheric ozone in the recent decades and its contribution to global
1010 total ozone, *J. Geophys. Res.-Atmos.*, 127, e2022JD037170. <https://doi.org/10.1029/2022JD037170>, 2022.
- 1011 Livesey, N. J., and Read, W. G.: Direct retrieval of line-of-sight atmospheric structure from limb sounding
1012 observations, *Geophys. Res. Lett.*, 27, 891-894, <https://doi.org/10.1029/1999GL010964>, 2000.
- 1013 Livesey, N. J., Van Snyder, W., Read, W. G., and Wagner, P. A.: Retrieval algorithms for the EOS Microwave Limb
1014 Sounder (MLS), *IEEE Trans. Geosci. Remote Sens.*, 44, 1144-1155, <https://doi.org/10.1109/TGRS.2006.872327>,
1015 2006.
- 1016 Livesey, N. J., Filipiak, M. J., Froidevaux, L., Read, W. G., Lambert, A., Santee, M. L., Jiang, J. H., Waters, J. W.,
1017 Cofield, R. E., Cuddy, D. T., Daffer, W. H., Drouin, B. J., Fuller, R. A., Jarnot, R. F., Jiang, Y. B., Knosp, B. W.,
1018 Li, Q. B., Perun, V. S., Schwartz, M. J., Snyder, W. V., Stek, P. C., Thurstans, R. P., Wagner, P. A., Pumphrey, H.
1019 C., Avery, M., Browell, E. V., Cammas, J.-P., Christensen, L. E., Edwards, D. P., Emmons, L. K., Gao, R.-S., Jost,
1020 H.-J., Loewenstein, M., Lopez, J. D., N'ed'elec, P., Osterman, G. B., Sachse, G. W., and Webster, C. R.: Validation
1021 of Aura Microwave Limb Sounder O₃ and CO observations in the upper troposphere and lower stratosphere, *J.*
1022 *Geophys. Res.*, 113, D15S02, <https://doi.org/10.1029/2007JD008805>, 2008.
- 1023 Livesey, N. J., Logan, J. A., Santee, M. L., Waters, J. W., Doherty, R. M., Read, W. G., Froidevaux, L., and Jiang, J.
1024 H.: Interrelated variations of O₃, CO and deep convection in the tropical/subtropical upper troposphere observed
1025 by the Aura Microwave Limb Sounder (MLS) during 2004-2011, *Atmos. Chem. Phys.*, 13, 579–598,
1026 <https://doi.org/10.5194/acp-13-579-2013>, 2013.
- 1027 Livesey, N. J., Read, W. G., Wagner, P. A., Froidevaux, L., Santee, M. L., Schwartz, M. J., Lambert, A., Millan Valle,
1028 L. F., Pumphrey, H. C., Manney, G. L., Fuller, R. A., Jarnot, R. F., Knosp, B. W., and Lay, R. R.: EOS MLS



- 1029 Version 5.0x Level 2 and 3 data quality and description document, Tech. rep., Jet Propulsion Laboratory D-105336
1030 Rev. B, Jan. 30, 2022, <https://mls.jpl.nasa.gov/publications>, 2022.
- 1031 Logan, Jennifer A.: Tropospheric ozone: Seasonal behavior, trends, and anthropogenic influence, *J. Geophys. Res.-*
1032 *Atmos.*, 90, 10463–10482, <https://doi.org/10.1029/JD090iD06p10463>, 1985.
- 1033 Logan, J. A., Prather, M. J., Wofsy, S. C., and McElroy, M. B.: Tropospheric chemistry: a global perspective, *J.*
1034 *Geophys. Res.*, 86, 7210–7254, <https://doi.org/10.1029/JC086iC08p07210>, 1981.
- 1035 Logan, J. A., Megretskaia, I., Nassar, R., Murray, L. T., Zhang, L., Bowman, K. W., Worden, H. M., and Luo, M.:
1036 Effects of the 2006 El Niño on tropospheric composition as revealed by data from the Tropospheric Emission
1037 Spectrometer (TES), *Geophys. Res. Lett.*, 35, L03816, <https://doi.org/10.1029/2007GL031698>, 2008.
- 1038 McDuffie, E. E., Smith, S. J., O'Rourke, P., Tibrewal, K., Venkataraman, C., Marais, E. A., Zheng, B., Crippa, M.,
1039 Brauer, M., and Martin, R. V.: A global anthropogenic emission inventory of atmospheric pollutants from sector-
1040 and fuel-specific sources (1970–2017): an application of the Community Emissions Data System (CEDS), *Earth*
1041 *Syst. Sci. Data*, 12, 3413–3442, <https://doi.org/10.5194/essd-12-3413-2020>, 2020.
- 1042 Meinshausen, M., Vogel, E., Nauels, A., Lorbacher, K., Meinshausen, N., Etheridge, D. M., Fraser, P. J., Montzka, S.
1043 A., Rayner, P. J., Trudinger, C. M., Krumme, P. B., Beyerle, U., Canadell, J. G., Daniel, J. S., Enting, I. G., Law,
1044 R. M., Lunder, C. R., O'Doherty, S., Prinn, R. G., Reimann, S., Rubino, M., Velders, G. J. M., Vollmer, M. K.,
1045 Wang, R. H.-J., and Weiss, R.: Historical greenhouse gas concentrations for climate modelling (CMIP6),
1046 *Geoscientific Model Development*, 10(5), 2057–2116. <https://doi.org/10.5194/gmd-10-2057-2017>, 2017.
- 1047 Meinshausen, M., Nicholls, Z. R. J., Lewis, J., Gidden, M. J., Vogel, E., Freund, M., Beyerle, U., Gessner, C., Nauels,
1048 A., Bauer, N., Canadell, J. G., Daniel, J. S., John, A., Krummel, P. B., Luderer, G., Meinshausen, N., Montzka, S.
1049 A., Rayner, P. J., Reimann, S., Smith, S. J., van den Berg, M., Velders, G. J. M., Vollmer, M. K., and Wang, R.
1050 H. J.: The shared socio-economic pathway (SSP) greenhouse gas concentrations and their extensions to 2500,
1051 *Geosci. Model Dev.*, 13, 3571–3605, <https://doi.org/10.5194/gmd-13-3571-2020>, 2020.
- 1052 Meul, S., Langematz, U., Kröger, P., Oberländer-Hayn, S., and Jöckel, P.: Future changes in the stratosphere-to-
1053 troposphere ozone mass flux and the contribution from climate change and ozone recovery, *Atmos. Chem. Phys.*,
1054 18, 7721–7738, <https://doi.org/10.5194/acp-18-7721-2018>, 2018.
- 1055 Miyazaki, K., Bowman, K., Sekiya, T., Takigawa, M., Neu, J. L., Sudo, K., Osterman, G., and Eskes, H.: Global
1056 tropospheric ozone responses to reduced NO_x emissions linked to the COVID-19 worldwide lockdowns, *Science*
1057 *Advances*, 7(24), eabf7460, <https://doi.org/10.1126/sciadv.abf7460>, 2021.
- 1058 Monks, P. S., Archibald, A. T., Colette, A., Cooper, O., Coyle, M., Derwent, R., Fowler, D., Granier, C., Law, K. S.,
1059 Mills, G. E., Stevenson, D. S., Tarasova, O., Thouret, V., von Schneidemesser, E., Sommariva, R., Wild, O., and
1060 Williams, M. L.: Tropospheric ozone and its precursors from the urban to the global scale from air quality to short-
1061 lived climate forcer, *Atmos. Chem. Phys.*, 15, 8889–8973, <https://doi.org/10.5194/acp-15-8889-2015>, 2015.
- 1062 Montzka, S. A., Krol, M., Dlugokencky, E., Hall, B., Jöckel, P., and Lelieveld, J.: Small Interannual Variability of
1063 Global Atmospheric Hydroxyl, *Science*, 331, 67–69, <https://doi.org/10.1126/science.1197640>, 2011.



- 1064 Murray, L. T., Mickley, L. J., Kaplan, J. O., Sofen, E. D., Pfeiffer, M., and Alexander, B.: Factors controlling
1065 variability in the oxidative capacity of the troposphere since the Last Glacial Maximum, *Atmos. Chem. Phys.*, 14,
1066 3589–3622, <https://doi.org/10.5194/acp-14-3589-2014>, 2014.
- 1067 Nassar, R., Logan, J. A., Megretskaia, I. A., Murray, L. T., Zhang, L., & Jones, D. B. A., Analysis of tropical
1068 tropospheric ozone, carbon monoxide, and water vapor during the 2006 El Niño using TES observations and the
1069 GEOS-Chem model, *J. Geophys. Res.-Atmos.*, 114, D17304, <https://doi.org/10.1029/2009jd011760>, 2009.
- 1070 Neely, R. R., and Schmidt, A.: VolcanEESM: Global volcanic sulphur dioxide (SO₂) emissions database from 1850
1071 to present - Version 1.0., <https://doi.org/10.5285/76ebdc0b-0eed-4f70-b89e-55e606bcd568>, 2016.
- 1072 Neu, J. L., Flury, T., Manney, G. L., Santee, M. L., Livesey, N. J., and Worden, J.: Tropospheric ozone variations
1073 governed by changes in stratospheric circulation, *Nat. Geosci.*, 7, 340–344, <https://doi.org/10.1038/ngeo2138>,
1074 2014.
- 1075 O’Neill, B. C., Tebaldi, C., van Vuuren, D. P., Eyring, V., Friedlingstein, P., Hurtt, G., Knutti, R., Kriegler, E.,
1076 Lamarque, J.-F., Lowe, J., Meehl, G. A., Moss, R., Riahi, K., and Sanderson, B. M.: The Scenario Model
1077 Intercomparison Project (Scenario MIP) for CMIP6, *Geosci. Model Dev.*, 9, 3461–3482,
1078 <https://doi.org/10.5194/gmd-9-3461-2016>, 2016.
- 1079 Oman, L. D., Ziemke, J. R., Douglass, A. R., Waugh, D. W., Lang, C., Rodriguez, J. M., and Nielsen, J. E.: The
1080 response of tropical tropospheric ozone to ENSO, *Geophys. Res. Lett.*, 38, L13706,
1081 <https://doi.org/10.1029/2011gl047865>, 2011.
- 1082 Oman, L. D., Douglass, A. R., Ziemke, J. R., Rodriguez, J. M., Waugh, D. W., and Nielsen, J. E.: The ozone response
1083 to ENSO in Aura satellite measurements and a chemistry-climate simulation, *J. Geophys. Res.*, 118, 965–976,
1084 <https://doi.org/10.1029/2012jd018546>, 2013.
- 1085 Park, M., Randel, W. J., Kinnison, D. E., Emmons, L. K., Bernath, P. F., and Walker, K. A., Boone, C. D., and Livesey,
1086 N. J.: Hydrocarbons in the upper troposphere and lower stratosphere observed from ACE-FTS and comparisons
1087 with WACCM, *J. Geophys. Res.-Atmos.*, 118, 1964–1980, <https://doi.org/10.1029/2012JD018327>, 2013.
- 1088 Park, K., Wang, Z., Emmons, L. K., and Mak, J. E.: Variation of atmospheric CO, δ¹³C, and δ¹⁸O at high northern
1089 latitude during 2004–2009: Observations and model simulations, *J. Geophys. Res.-Atmos.*, 120, 11,024–11,036,
1090 <https://doi.org/10.1002/2015JD023191>, 2015.
- 1091 Park, M., Worden, H. M., Kinnison, D. E., Gaubert, B., Tilmes, S., Emmons, L. K., Santee, M. L., Froidevaux, L.,
1092 and Boone, C. D.: Fate of pollution emitted during the 2015 Indonesian fire season, *J. Geophys. Res.-Atmos.*, 126,
1093 e2020JD033474, <https://doi.org/10.1029/2020JD033474>, 2021.
- 1094 Patel, A., Mallika, C., Chandrab, N., Patrab, P. K., Steinbacher, M., Revisiting regional and seasonal variations in
1095 decadal carbon monoxide variability: Global reversal of growth rate, *Science of the Total Environment*, 909,
1096 168476, <https://doi.org/10.1016/j.scitotenv.2023.168476>, 2024.
- 1097 Petzold, A., Thouret, V., Gerbig, C., Zahn, A., Brenninkmeijer, C. A. M., Gallagher, M., Hermann, M., Pontaud, M.,
1098 Ziereis, H., Boulanger, D., Marshall, J., Nédélec, P., Smit, H. G. J., Friess, U., Flaud, J.-M., Wahner, A., Cammas,
1099 J.-P., and Volz-Thomas, A.: Global-scale atmosphere monitoring by in-service aircraft – current achievements and



- 1100 future prospects of the European Research Infrastructure IAGOS, *Tellus B*, 67, 28452,
1101 <https://doi.org/10.3402/tellusb.v67.28452>, 2015.
- 1102 Randel, W. J., Park, M., Wu, F., and Livesey, N. J.: A large annual cycle in ozone above the tropical tropopause linked
1103 to the Brewer-Dobson circulation, *J. Atmos. Sci.*, 64, 4479–4488, <https://doi.org/10.1175/2007JAS2409.1>, 2007.
- 1104 Read, W. G., Shippony, Z., and Snyder, W. V.: The clear-sky unpolarized forward model for the EOS Aura microwave
1105 limb sounder (MLS), *IEEE Trans. Geosci. Remote Sens.*, 44, 1367–1379,
1106 <https://doi.org/10.1109/TGRS.2006.862267>, 2006.
- 1107 Riahi, K., van Vuuren, D. P., Kriegler, E., Edmonds, J., O'Neill, B. C., Fujimori, S., Bauer, N., Calvin, K., Dellink,
1108 R., Fricko, O., Lutz, W., Popp, A., Crespo Cuaresma, J., Samir, K. C., Leimbach, M., Jiang, L., Kram, T., Rao, S.,
1109 Emmerling, J., Ebi, K., Hasegawa, T., Havlik, P., Humpenöder, F., Da Silva, A., Smith, S., Stehfest, E., Bosetti,
1110 V., Eom, J., Gernaat, D., Masui, T., Rogelj, J., Strefler, J., Drouet, L., Krey, V., Luderer, G., Harmsen, M.,
1111 Takahashi, K., Baumstark, L., Doelman, J. C., Kainuma, M., Klimont, Z., Marangoni, G., Lotze-Campen, H.,
1112 Obersteiner, M., Tabeau, A., Tavoni, M.: The Shared Socioeconomic Pathways and their energy, land use, and
1113 greenhouse gas emissions implications: An overview, *Global Environ. Chang.*, 42, 1045–1068,
1114 <https://doi.org/10.1016/j.gloenvcha.2016.05.009>, 2017.
- 1115 Rodgers, C.: *Inverse Methods for Atmospheric Sounding: Theory and Practice*, Vol. 2 of Series on Atmospheric,
1116 Oceanic and Planetary Physics, World Scientific, Singapore, 2000.
- 1117 Rowlinson, M. J., Rap, A., Arnold, S. R., Pope, R. J., Chipperfield, M. P., McNorton, J., Forster, P., Gordon, H.,
1118 Pringle, K. J., Feng, W., Kerridge, B. J., Latter, B. L., and Siddans, R.: Impact of El Niño–Southern Oscillation on
1119 the interannual variability of methane and tropospheric ozone, *Atmos. Chem. Phys.*, 19, 8669–8686,
1120 <https://doi.org/10.5194/acp-19-8669-2019>, 2019.
- 1121 Schoeberl, M. R., Duncan, B. N., Douglass, A. R., Waters, J., Livesey, N., Read, W., and Filipiak, M.: The carbon
1122 monoxide tape recorder, *Geophys. Res. Lett.*, 33, L12811, <https://doi.org/10.1029/2006gl026178>, 2006.
- 1123 Schumann, U. and Huntrieser, H.: The global lightning-induced nitrogen oxides source, *Atmos. Chem. Phys.*, 7, 3823–
1124 3907, <https://doi.org/10.5194/acp-7-3823-2007>, 2007.
- 1125 Soulié, A., Granier, C., Darras, S., Zilbermann, N., Doumbia, T., Guevara, M., Jalkanen, J.-P., Keita, S., Liousse, C.,
1126 Crippa, M., Guizzardi, D., Hoesly, R., and Smith, S.: Global Anthropogenic Emissions (CAMSGLOBANT) for
1127 the Copernicus Atmosphere Monitoring Service Simulations of Air Quality Forecasts and Reanalyses, *Earth Syst.*
1128 *Sci. Data Discuss.* [preprint], <https://doi.org/10.5194/essd-2023-306>, in review, 2023.
- 1129 Souri, A. H., Choi, Y., Jeon, W., Woo, J.-H., Zhang, Q., and Kurokawa, J.: Remote sensing evidence of decadal
1130 changes in major tropospheric ozone precursors over East Asia, *J. Geophys. Res.-Atmos.*, 122, 2474–2492,
1131 <https://doi.org/10.1002/2016JD025663>, 2017.
- 1132 SPARC: The SPARC Data Initiative: Assessment of stratospheric trace gas and aerosol climatologies from satellite
1133 limb sounders, M. I. Hegglin and S. Tegtmeier (eds.), SPARC Report No. 8, WCRP-5/2017, available at
1134 www.sparc-climate.org/publications/sparc-reports/, 2017.



- 1135 Stein, O., M. G. Schultz, M. G., Bouarar, I., Clark, H., Huijnen, V., A. Gaudel, A., George, M., and Clerbaux, C.: On
1136 the wintertime low bias of Northern Hemisphere carbon monoxide found in global model simulations, *Atmos.*
1137 *Chem. Phys.*, 14, 9295–9316, <https://doi.org/10.5194/acp-14-9295-2014>, 2014.
- 1138 Steinbrecht, W., Kubistin, D., Plass-Dülmer, C., Davies, J., Tarasick, D. W., Gathen, P. v. d., Deckelmann, H., Jepsen,
1139 N., Kivi, R., Lyall, N., Palm, M., Notholt, J., Kois, B., Oelsner, P., Allaart, M., PETERS, A., Gill, M., Van Malderen,
1140 R., Delcloo, A. W., Sussmann, R., Mahieu, E., Servais, C., Romanens, G., Stübi, R., Ancellet, G., Godin-
1141 Beekmann, S., Yamanouchi, S., Strong, K., Johnson, B., Cullis, P., Petropavlovskikh, I., Hannigan, J. W.,
1142 Hernandez, J.-L., Diaz Rodriguez, A., Nakano, T., Chouza, F., Leblanc, T., Torres, C., Garcia, O., Röhling, A. N.,
1143 Schneider, M., Blumenstock, T., Tully, M., Paton-Walsh, C., Jones, N., Querel, R., Strahan, S., Stauffer, R. M.,
1144 Thompson, A. M., Inness, A., Engelen, R., Chang, K.-L., and Cooper, O. R.: COVID-19 Crisis Reduces Free
1145 Tropospheric Ozone Across the Northern Hemisphere, *Geophys. Res. Lett.*, 48, e2020GL091987,
1146 <https://doi.org/10.1029/2020GL091987>, 2021.
- 1147 Stevenson, D. S., Young, P. J., Naik, V., Lamarque, J.-F., Shindell, D. T., Voulgarakis, A., Skeie, R. B., Dalsoren, S.
1148 B., Myhre, G., Berntsen, T. K., Folberth, G. A., Rumbold, S. T., Collins, W. J., MacKenzie, I. A., Doherty, R. M.,
1149 Zeng, G., van Noije, T. P. C., Strunk, A., Bergmann, D., Cameron-Smith, P., Plummer, D. A., Strode, S. A.,
1150 Horowitz, L., Lee, Y. H., Szopa, S., Sudo, K., Nagashima, T., Josse, B., Cionni, I., Righi, M., Eyring, V., Conley,
1151 A., Bowman, K. W., Wild, O., and Archibald, A.: Tropospheric ozone changes, radiative forcing and attribution
1152 to emissions in the Atmospheric Chemistry and Climate Model Intercomparison Project (ACCMIP), *Atmos.*
1153 *Chem. Phys.*, 13, 3063–3085, <https://doi.org/10.5194/acp-13-3063-2013>, 2013.
- 1154 Strode, S. A., Worden, H. M., Damon, M., Douglass, A. R., Duncan, B. N., Emmons, L. K., Lamarque, J.-F., Manyin,
1155 M., Oman, L. D., Rodriguez, J. M., Strahan, S. E., and Tilmes, S.: Interpreting space-based trends in carbon
1156 monoxide with multiple models, *Atmos. Chem. Phys.*, 16, 7285–7294, <https://doi.org/10.5194/acp-16-7285-2016>,
1157 2016.
- 1158 Sudo, K. and Takahashi, M.: Simulation of tropospheric ozone changes during 1997–1998 El Niño: Meteorological
1159 impact on tropospheric photochemistry, *Geophys. Res. Lett.*, 28, 4091–4094,
1160 <https://doi.org/10.1029/2001GL013335>, 2001.
- 1161 Sudo, K., Takahashi, M., and Akimoto, H.: Future changes in stratosphere-troposphere exchange and their impacts on
1162 future tropospheric ozone simulations, *Geophys. Res. Lett.*, 30, 24, 2256, <https://doi.org/10.1029/2003GL018526>
1163 , 2003.
- 1164 Tapping, K.F.: The 10.7 cm solar radio flux (F10.7), *Space Weather*, 11, 394-406, <https://doi.org/10.1002/swe.20064>,
1165 2013.
- 1166 Thompson, A. M., Doddridge, B. G., Witte, J. C., Hudson, R. D., Luke, W. T., Johnson, J. E., Johnson, B. J., Oltmans,
1167 S. J., and Weller, R.: A tropical Atlantic ozone paradox: Shipboard and satellite views of a tropospheric ozone
1168 maximum and wave-one in January–February 1999, *Geophys. Res. Lett.*, 27, 3317–3320,
1169 <https://doi.org/10.1029/1999GL011273>, 2000.
- 1170 Thompson, A. M., Witte, J. C., Oltmans, S. J., Schmidlin, F. J., Logan, J. A., Fujiwara, M., Kirchhoff, V. W. J., Posny,
1171 F., Coetzee, G. J. R., Hoegger, B., Kawakami, S., Ogawa, T., Fortuin, J. P. F., and Kelder, H. M.: Southern



- 1172 Hemisphere Additional Ozonesondes (SHADOZ) 1998–2000 tropical ozone climatology. 2. Tropospheric
1173 variability and the zonal wave-one, *J. Geophys. Res.-Atmos.*, 108(D2), 8241,
1174 <https://doi.org/10.1029/2002JD002241>, 2003.
- 1175 Thompson, A. M., Stauffer, R. M., Wargan, K., Witte, J. C., Kollonige, D. E., and Ziemke, J. R.: Regional and
1176 seasonal trends in tropical ozone from SHADOZ profiles: Reference for models and satellite products, *J. Geophys.*
1177 *Res.-Atmos.*, **126**, e2021JD034691, <https://doi.org/10.1029/2021JD034691>, 2021.
- 1178 Tilmes, S., Hodzic, A., Emmons, L. K., Mills, M. J., Gettelman, A., Kinnison, D. E., Park, M., Lamarque, J.-F., Vitt,
1179 F., Shrivastava, M., Campuzano-Jost, P., Jimenez, J. L., and Liu, X.: Climate forcing and trends of organic
1180 aerosols in the Community Earth System Model (CESM2), *J. of Adv. in Modeling Earth Systems*, 11, 4323–4351,
1181 <https://doi.org/10.1029/2019MS001827>, 2019.
- 1182 Tsvilidou, M., Sauvage, B., Bennouna, Y., Blot, R., Boulanger, D., Clark, H., Le Flochmoën, E., Nédélec, P., Valérie
1183 Thouret, V., Wolff, P., and Barret, B.: Tropical tropospheric ozone and carbon monoxide distributions:
1184 characteristics, origins, and control factors, as seen by IAGOS and IASI, *Atmos. Chem. Phys.*, 23, 14039–14063,
1185 <https://doi.org/10.5194/acp-23-14039-2023>, 2023.
- 1186 Voulgarakis, A., Marlier, M. E., Faluvegi, G., Shindell, D. T., Tsigaridis, K., and Mangeon, S.: Interannual variability
1187 of tropospheric trace gases and aerosols: The role of biomass burning emissions, *J. Geophys. Res.-Atmos.*, 120,
1188 7157–7173, <https://doi.org/10.1002/2014JD022926>, 2015.
- 1189 Wang, P.-H., Fishman, J., Harvey, V. L., and Hitchman, M. H.: Southern tropical upper tropospheric zonal ozone
1190 wave-1 from SAGE II observations (1985–2002), *J. Geophys. Res.-Atmos.*, 111, D08305,
1191 <https://doi.org/10.1029/2005JD006221>, 2006.
- 1192 Wang, H., Lu, X., Jacob, D. J., Cooper, O. R., Chang, K.-L., Li, K., Gao, M., Liu, Y., Sheng, B., Wu, K., Wu, T.,
1193 Zhang, J., Sauvage, B., Nédélec, P., Blot, R., and Fan, S.: Global tropospheric ozone trends, attributions, and
1194 radiative impacts in 1995–2017: an integrated analysis using aircraft (IAGOS) observations, ozonesonde, and
1195 multi-decadal chemical model simulations, *Atmos. Chem. Phys.*, 22, 13753–13782, [https://doi.org/10.5194/acp-](https://doi.org/10.5194/acp-22-13753-2022)
1196 [22-13753-2022](https://doi.org/10.5194/acp-22-13753-2022), 2022.
- 1197 Warner, J., Carminati, F., Wei, Z., Lahoz, W., and Attié, J.-L.: Tropospheric carbon monoxide variability from AIRS
1198 under clear and cloudy conditions, *Atmos. Chem. Phys.*, 13, 12469–12479, [https://doi.org/10.5194/acp-13-12469-](https://doi.org/10.5194/acp-13-12469-2013)
1199 [2013](https://doi.org/10.5194/acp-13-12469-2013), 2013.
- 1200 Waters, J., Froidevaux, L., Harwood, R., Jarnot, R., Pickett, H., Read, W., Siegel, P., Cofield, R., Filipiak, M., Flower,
1201 D., Holden, J., Lau, G., Livesey, N., Manney, G., Pumphrey, H., Santee, M., Wu, D., Cuddy, D., Lay, R., Loo, M.,
1202 Perun, V., Schwartz, M., Stek, P., Thurstans, R., Boyles, M., Chandra, S., Chavez, M., Chen, G.-S., Chudasama,
1203 B., Dodge, R., Fuller, R., Girard, M., Jiang, J., Jiang, Y., Knosp, B., LaBelle, R., Lam, J., Lee, K., Miller, D.,
1204 Oswald, J., Patel, N., Pukala, D., Quintero, O., Scaff, D., Snyder, V., Tope, M., Wagner, P., and Walch, M.: The
1205 Earth Observing System Microwave Limb Sounder (EOS MLS) on the Aura satellite, *IEEE Transac. Geosci.*
1206 *Remote Sens.*, 44, 5, <https://doi.org/10.1109/TGRS.2006.873771>, 2006.
- 1207 Witte, J. C., Schoeberl, M. R., Douglass, A. R., and Thompson, A. M.: The quasi-biennial oscillation in tropical ozone
1208 from SHADOZ and HALOE, *Atmos. Chem. Phys.*, 8, 3929–3936, <https://doi.org/10.5194/acp-8-3929-2008>, 2008.



- 1209 Wolter, K., and Timlin, M. S.: El Niño/Southern Oscillation behaviour since 1871 as diagnosed in an extended
1210 multivariate ENSO index (MEI.ext), *Intl. J. Climatology*, 31, 1074–1087, <https://doi.org/10.1002/joc.2336>, 2011.
- 1211 Worden, H. M., Deeter, M. N., Frankenberg, C., George, M., Nichitiu, F., Worden, J., Aben, I., Bowman, K. W.,
1212 Clerbaux, C., Coheur, P. F., de Laat, A. T. J., Detweiler, R., Drummond, J. R., Edwards, D. P., Gille, J. C.,
1213 Hurtmans, D., Luo, M., Martinez- Alonso, S., Massie, S., Pfister, G., and Warner, J. X.: Decadal record of satellite
1214 carbon monoxide observations, *Atmos. Chem. Phys.*, 13, 837–850, <https://doi.org/10.5194/acp-13-837-2013>,
1215 2013a.
- 1216 Worden, J., Wecht, K., Frankenberg, C., Alvarado, M., Bowman, K., Kort, E., Kulawik, S., Lee, M., Payne, V., and
1217 Worden, H.: CH₄ and CO distributions over tropical fires during October 2006 as observed by the Aura TES
1218 satellite instrument and modeled by GEOS-Chem, *Atmos. Chem. Phys.*, 13, 3679–3692,
1219 <https://doi.org/10.5194/acp-13-3679-2013>, 2013b.
- 1220 Yoon, J., and Pozzer, A.: Model-simulated trend of surface carbon monoxide for the 2001–2010 decade, *Atmos.*
1221 *Chem. Phys.*, 14, 10465–10482, <https://doi.org/10.5194/acp-14-10465-2014>, 2014.
- 1222 Zhang, L., Li, Q. B., Jin, J., Liu, H., Livesey, N., Jiang, J. H., Mao, Y., Chen, D., Luo, M., and Chen, Y.: Impacts of
1223 2006 Indonesian fires and dynamics on tropical upper tropospheric carbon monoxide and ozone, *Atmos. Chem.*
1224 *Phys.*, 11, 10929–10946, <https://doi.org/10.5194/acp-11-10929-2011>, 2011.
- 1225 Zhang, S., Zhao, P., He, L., Yang, Y., Liu, B., He, W., Cheng, Y., Liu, Y., Liu, S., Hu, Q., Huang, C., Wu, Y., On-
1226 board monitoring (OBM) for heavy-duty vehicle emissions in China: Regulations, early-stage evaluation and
1227 policy recommendations, *Science of the Total Environment*, Vol. 731, 139045, ISSN 0048-9697,
1228 <https://doi.org/10.1016/j.scitotenv.2020.139045>, 2020.
- 1229 Zhang, T., Hoell, A., Perlwitz, J., Eischeid, J., Murray, D., Hoerling, M., and Hamill, T.: Towards Probabilistic
1230 Multivariate ENSO Monitoring, *Geophys. Res. Lett.*, 46, <https://doi.org/10.1029/2019GL083946>, 2019.
- 1231 Zhang, Y., Cooper, O. R., Gaudel, A., Thompson, A. M., Nédélec, P., Ogino, S.-Y., and West, J. J.: Tropospheric
1232 ozone change from 1980 to 2010 dominated by equatorward redistribution of emissions, *Nat. Geosci.*, 9, 875–879,
1233 <https://doi.org/10.1038/ngeo2827>, 2016.
- 1234 Zheng, B., Chevallier, F., Ciais, P., Yin, Y., Deeter, M. N., Worden, H. M., Wang, Y., Zhang, Q., and He, K.: Rapid
1235 decline in carbon monoxide emissions and export from East Asia between years 2005 and 2016, *Environ. Res.*
1236 *Lett.*, 13, 044007, <https://doi.org/10.1088/1748-9326/aab2b3>, 2018.
- 1237 Ziemke, J. R., and Chandra, S.: La Niña and El Niño–induced variabilities of ozone in the tropical lower atmosphere
1238 during 1970–2001, *Geophys. Res. Lett.*, 30, 3, 1142, <https://doi.org/10.1029/2002GL016387>, 2003.
- 1239 Ziemke, J. R., Chandra, S., Oman, L. D., and Bhartia, P. K.: A new ENSO index derived from satellite measurements
1240 of column ozone, *Atmos. Chem. Phys.*, 10, 3711–3721, <https://doi.org/10.5194/acp-10-3711-2010>, 2010.
- 1241 Ziemke, J. R., A. R. Douglass, A. R., L. D. Oman, L. D., S. E. Strahan, S. E., and B. N. Duncan, B. N.: Tropospheric
1242 ozone variability in the tropics from ENSO to MJO and shorter timescales, *Atmos. Chem. Phys.*, 15, 8037–8049,
1243 <https://doi.org/10.5194/acp-15-8037-2015>, 2015.
- 1244 Ziemke, J. R., Oman, L. D., Strode, S. A., Douglass, A. R., Olsen, M. A., McPeters, R. D., Bhartia, P. K., Froidevaux,
1245 L., Labow, G. J., Witte, J. C., Thompson, A. M., Haffner, D. P., Kramarova, N. A., Frith, S. M., Huang, L.-K.,



- 1246 Jaross, G. R., Seftor, C. J., Deland, M. T., and Taylor, S. L.: Trends in global tropospheric ozone inferred from a
1247 composite record of TOMS/OMI/MLS/OMPS satellite measurements and the MERRA-2 GMI simulation, Atmos.
1248 Chem. Phys., 19, 3257–3269, <https://doi.org/10.5194/acp-19-3257-2019>, 2019.
- 1249 Ziemke, J. R., Kramarova, N. A., Frith, S. M., Huang, L.-K., Haffner, D. P., and Wargan, K.: NASA satellite
1250 measurements show global-scale reductions in free tropospheric ozone in 2020 and again in 2021 during COVID-
1251 19, Geophys. Res. Lett., 49, e2022GL098712, <https://doi.org/10.1029/2022GL098712>, 2022.
- 1252



1253 **Table 1.** Some characteristics of the three chemistry climate models used in this work.

1254

Model Designation	CO Anthropogenic Emissions dataset	CO Biomass Burning dataset	Nudging timescale (hours)	Tropical Lightning NO_x (Tg N yr⁻¹)	Aircraft NO_x Dataset¹
CAM-chem	CAMS-GLOB-ANT_v5.1	QFED	6	2.85	CAMS-GLOB-AIR_v2.1
CAM-chem-CEDS	CEDSv2	QFED	6	2.85	CAMS-GLOB-AIR_v2.1
WACCM	CEDSv2	QFED	12	3.52	CMIP6

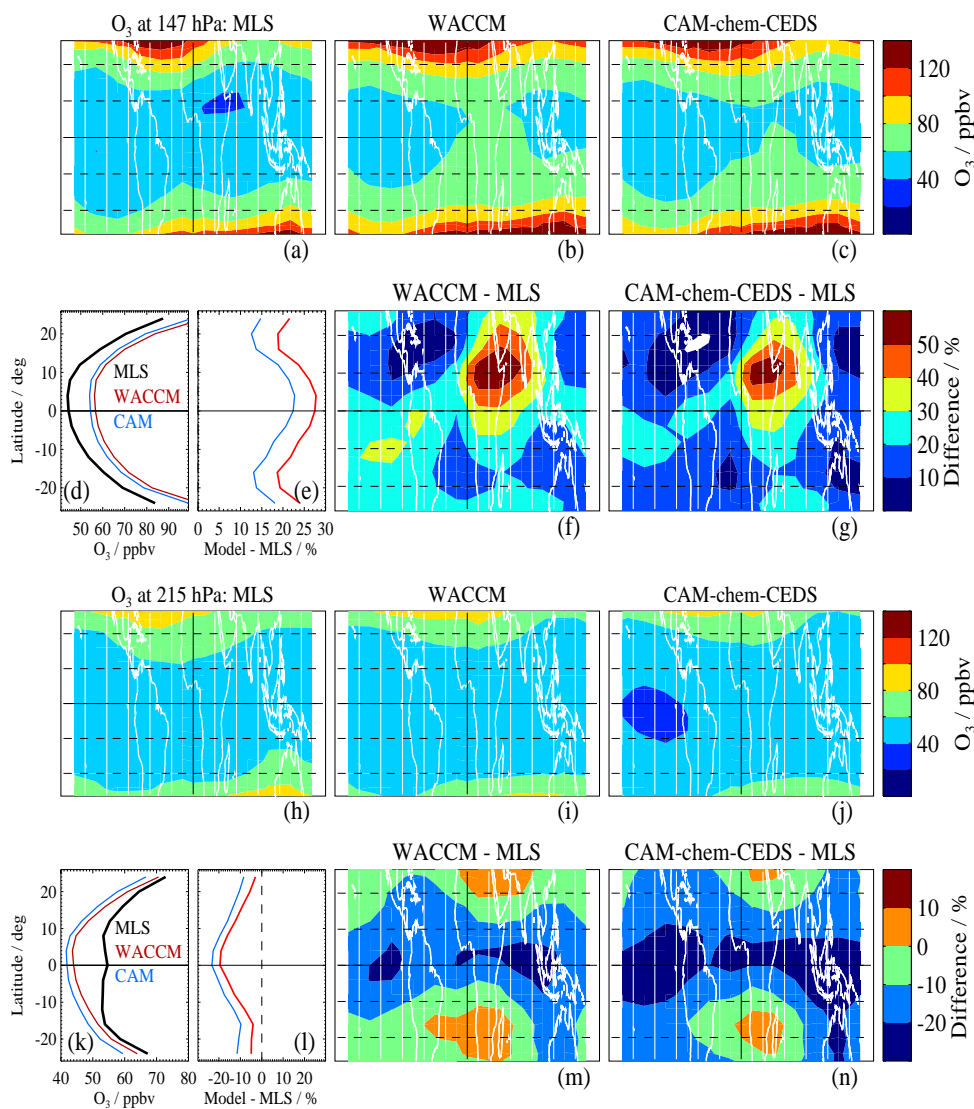
1255

1256 ¹For 2005–2014, the aircraft NO_x emissions for WACCM and the CAM-chem models are
1257 identical. From 2015 onward, the WACCM emissions are kept constant.

1258



1259 **Figures**
 1260
 1261



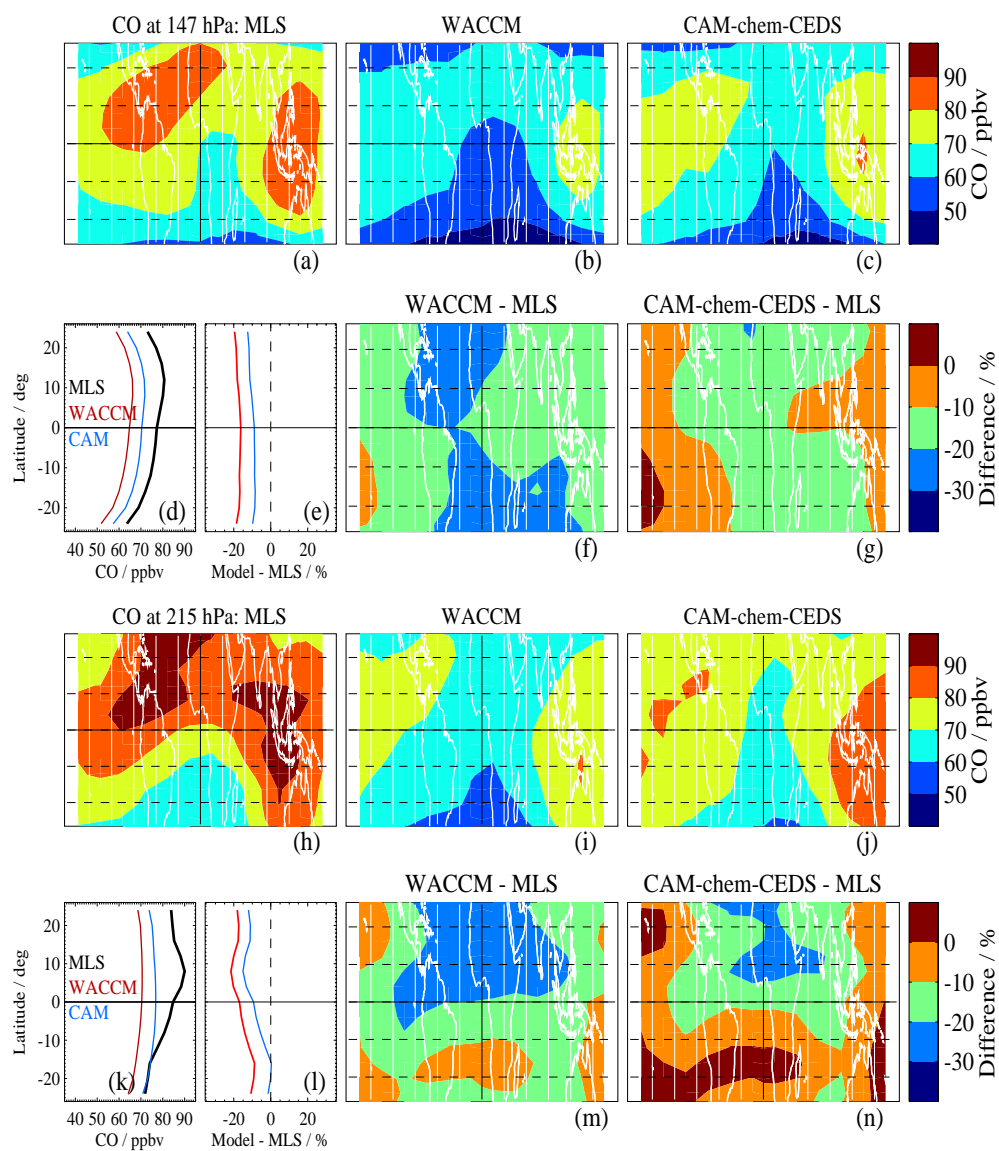
1262
 1263
 1264
 1265
 1266
 1267
 1268
 1269
 1270
 1271
 1272

Figure 1. Annually-averaged climatological comparisons between MLS and model ozone fields for 2005-2020 at low latitudes (26°S to 26°N) at 147 hPa ((a) through (g)) and at 215 hPa ((h) through (n)). For 147 hPa: (a) climatological O₃ maps from MLS, (b) from WACCM, (c) from CAM-chem-CEDS; (d) shows the zonal mean climatology from the MLS data and both models, with (e) giving the differences in zonal means for both models minus MLS (color-coded as shown in the (d) legend), while (f) provides a difference map of the climatologies from WACCM minus MLS, and (g) gives the difference map for CAM-chem-CEDS minus MLS. Panels (h) through (n) provide the same information as (a) through (g), but for 215 hPa.



1273

1274



1275

1276

1277

1278

1279

1280

1281

1282

1283

1284

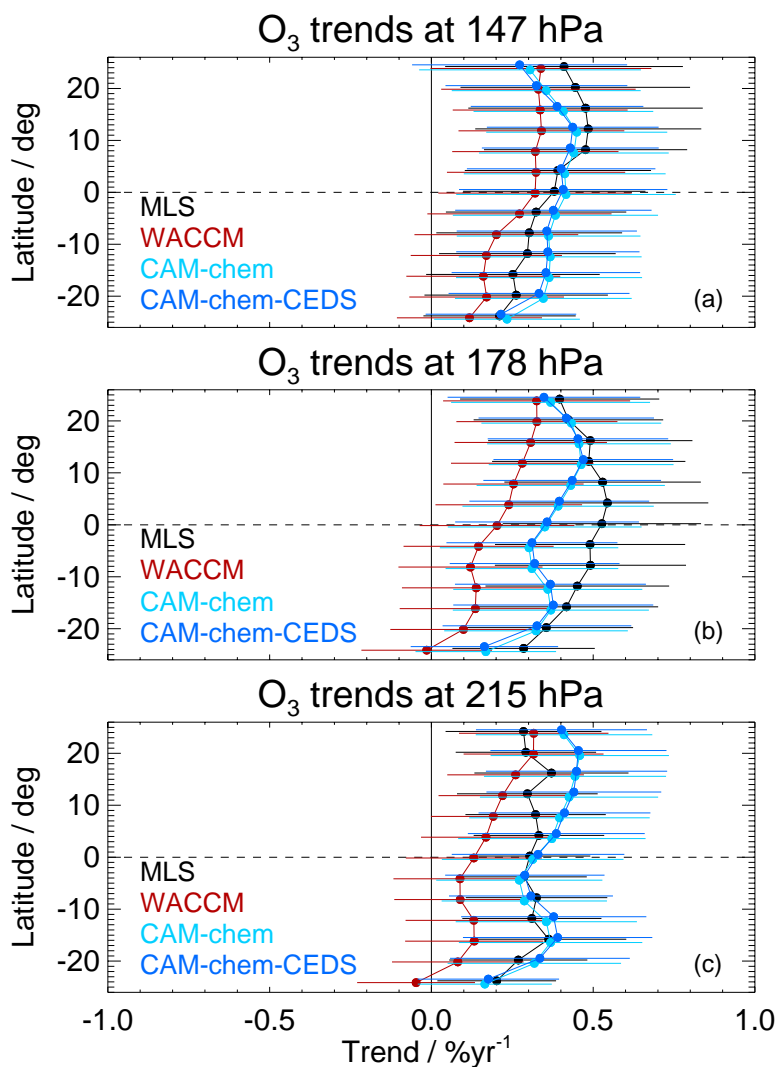
1285

Figure 2. Same as Fig. 1, but for CO.



1286

1287



1288

1289

1290

1291

1292

1293

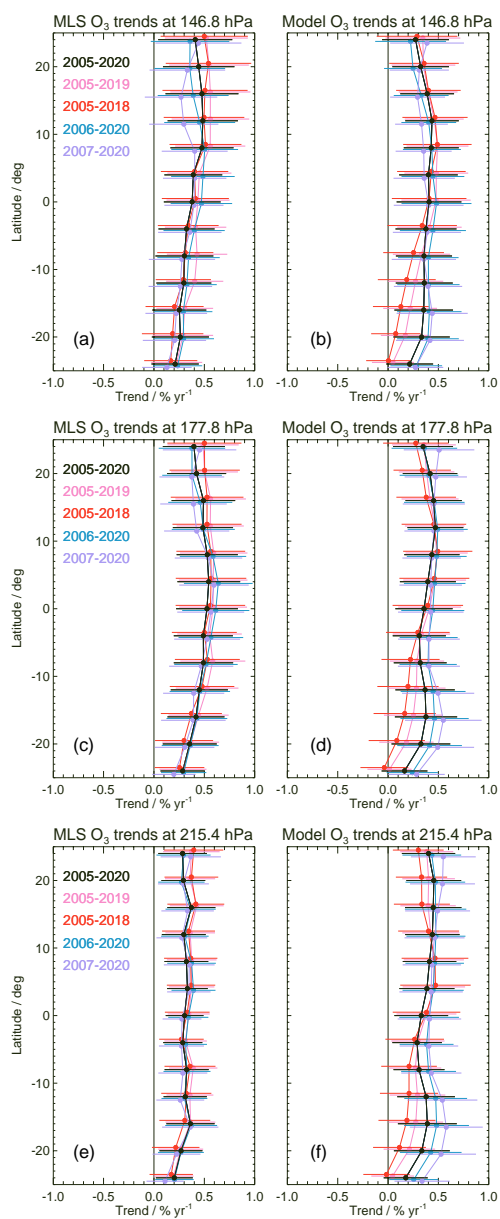
1294

1295

1296

1297

Figure 3. Ozone zonal mean trends versus latitude in the tropical upper troposphere, for 2005–2020, based on MLR analyses of time series from MLS (black), WACCM (red), CAM-chem (cyan) and CAM-chem-CEDS (blue). Each row corresponds to a different pressure level: (a) for 147 hPa, (b) for 178 hPa, and (c) for 215 hPa, as labeled above each panel. Error bars give the uncertainties (2σ) in the estimated linear trends (see text for more details).

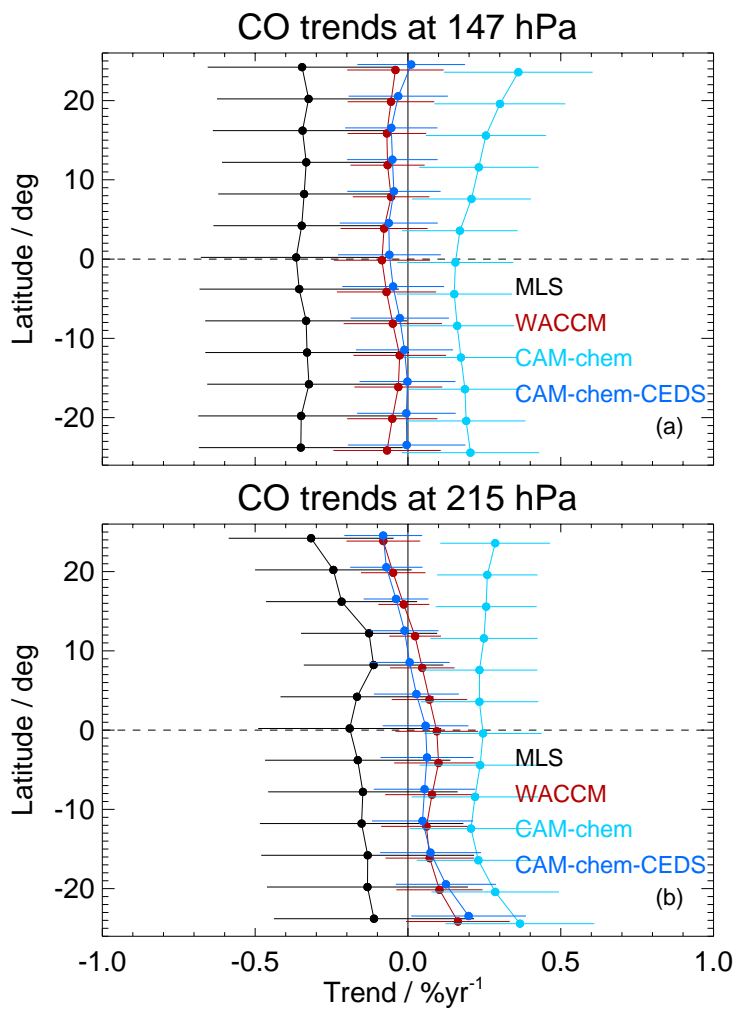


1298
1299
1300
1301
1302
1303
1304
1305
1306
1307

Figure 4. Ozone zonal mean trends versus latitude in the tropical upper troposphere, with results from MLS data analyses shown in the left panels, and model results from CAM-chem-CEDS in the right panels. Each row corresponds to a different pressure level, as labeled. All panels show the trend sensitivity to the time period used in the regression fits. For example, black is used to show the period from 2005 through 2020; results from four other time periods are also shown, with the start or end year shifted by one or two years (see legend for the meaning of the various colors). The error bars given here represent the (2σ) uncertainties in the estimated linear trends.



1308

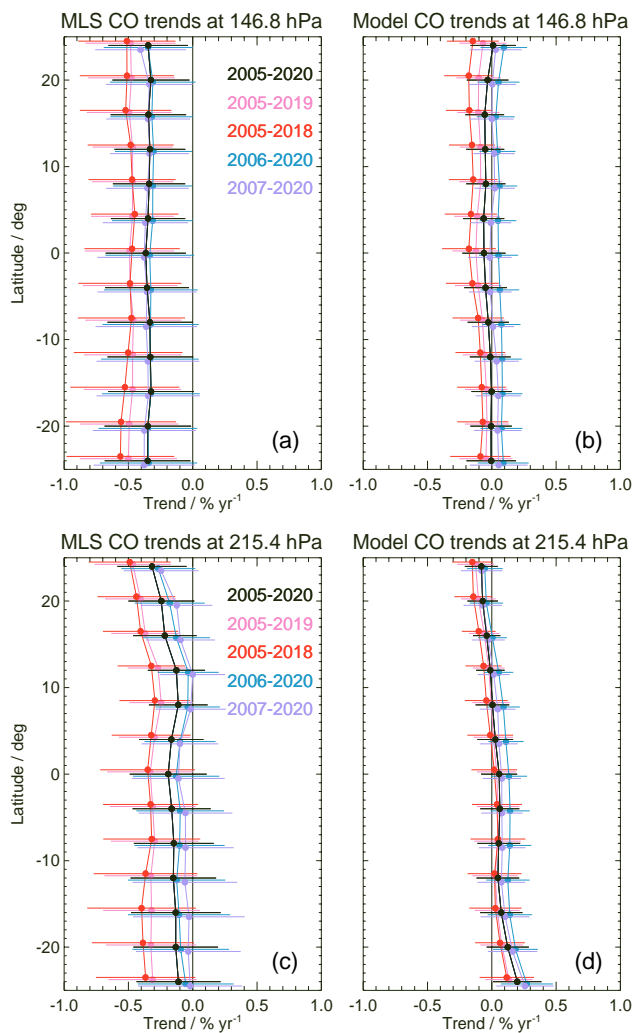


1309
1310
1311
1312
1313

Figure 5. Same as Fig. 3, but for CO zonal mean trends for (a) 147 hPa, and (b) 215 hPa.



1314
1315
1316
1317
1318
1319

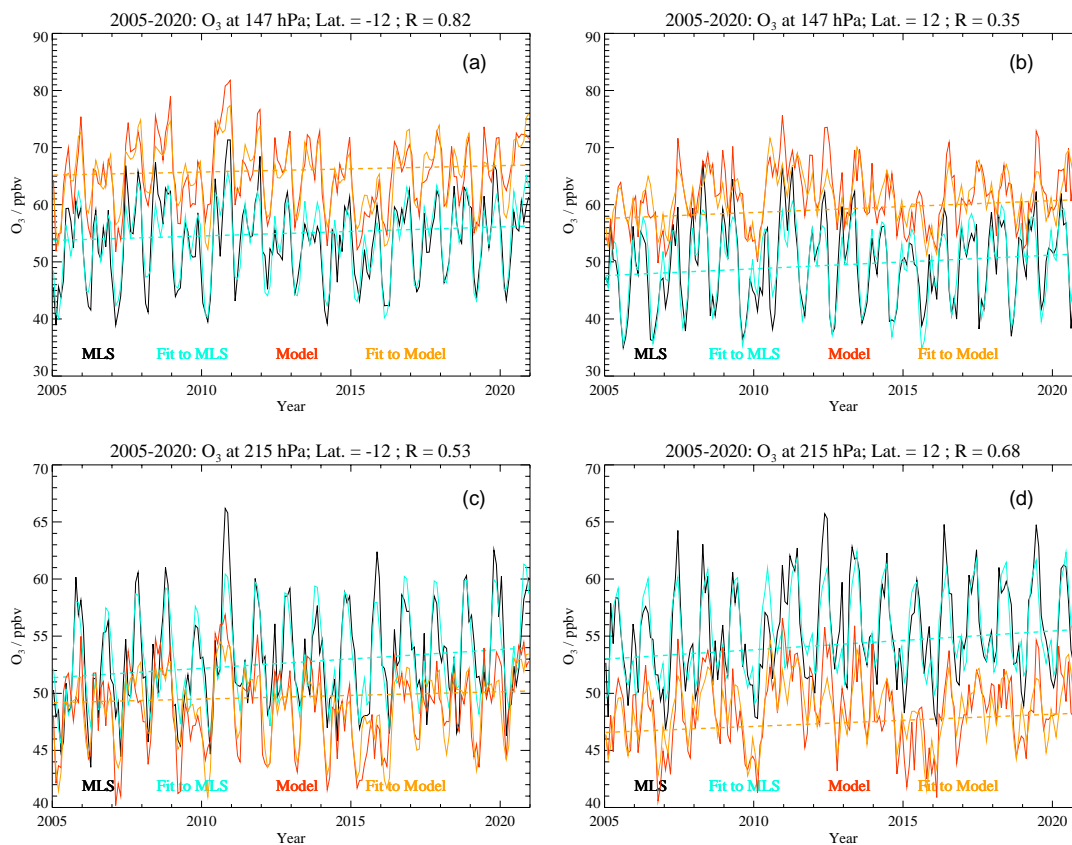


1320
1321
1322
1323

Figure 6. Same as Fig. 4, but for CO tropical zonal mean trends from MLS and CAM-chem-CEDS at the MLS CO UT retrieval levels of 147 and 215 hPa.



1324

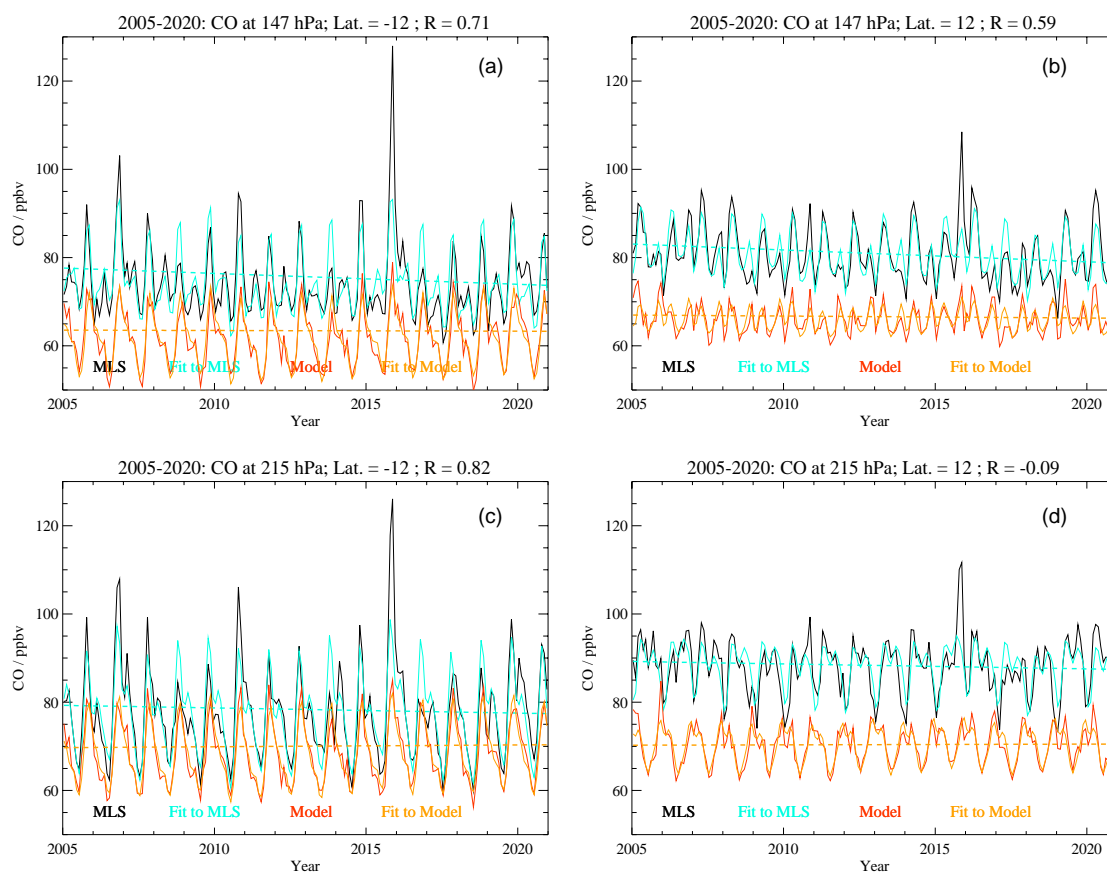


1325
1326

1327 **Figure 7.** Examples of MLS and model (WACCM) O₃ monthly zonal mean time series (2005–2020) for
1328 (a) 147 hPa and 12°S (meaning 10°S to 14°S), (b) 147 hPa and 12°N, (c) 215 hPa and 12°S, and (d) 215
1329 hPa and 12°N. The MLS data (black) are fitted by the MLR model (shown in cyan), and the WACCM series
1330 (red) are fitted by the same type of regression model (orange). The cyan and orange dashed lines are the
1331 linear components of the regression fits for the MLS and WACCM curves, respectively. The correlation
1332 coefficient values (R) for the WACCM versus MLS series are shown above each panel.
1333



1334
1335



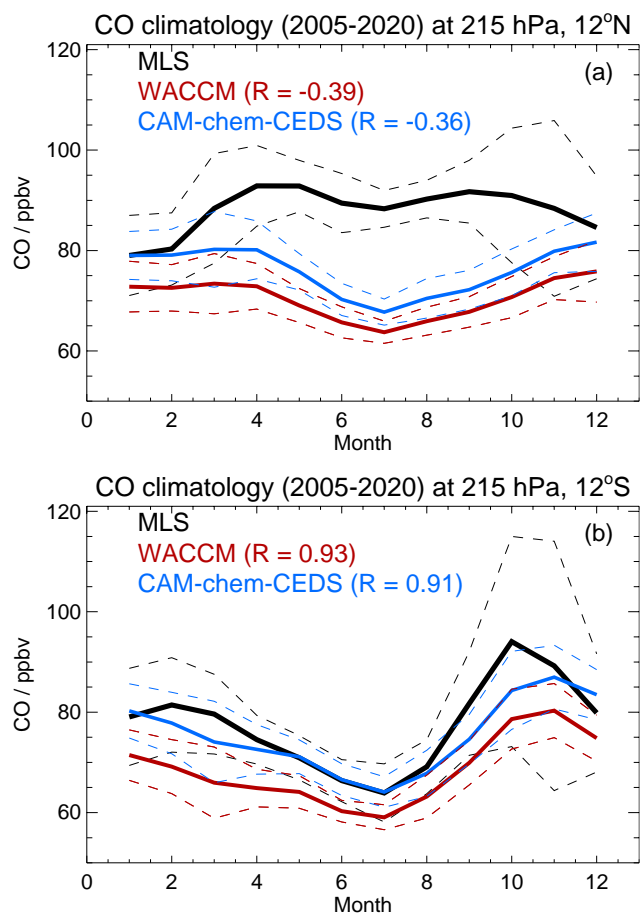
1336
1337
1338
1339

Figure 8. Same as Fig. 7, but for CO.



1340

1341



1342

1343

1344

1345

1346

1347

1348

1349

1350

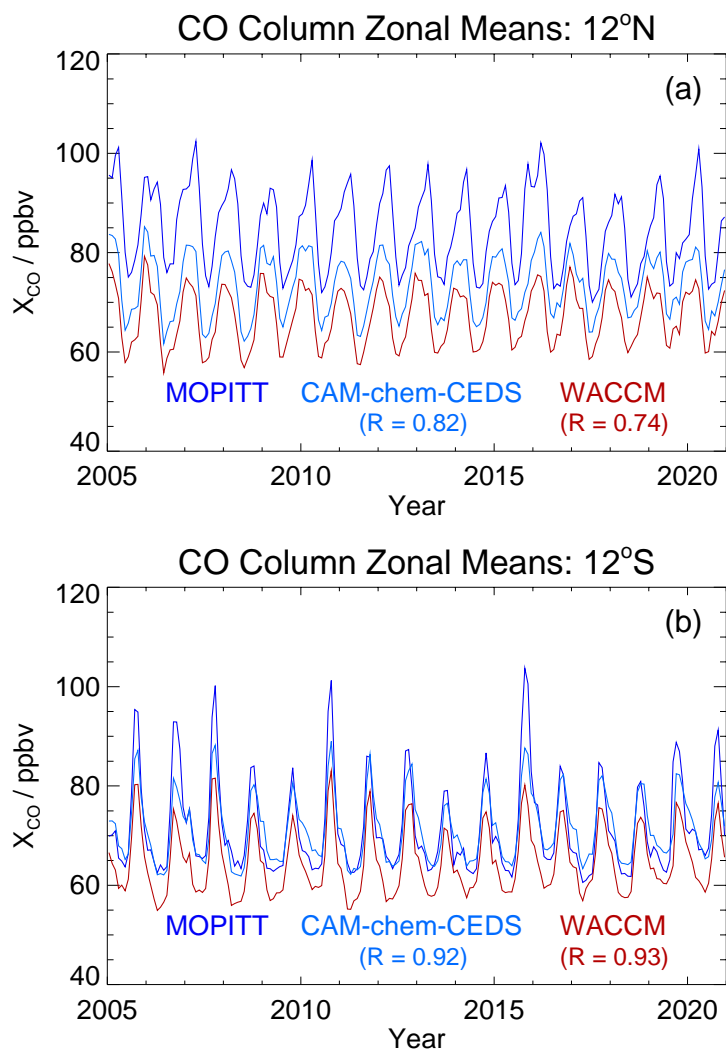
1351

1352

1353

1354

Figure 9. CO climatology at 215 hPa (using the 2005–2020 period) from MLS, WACCM, and CAM-chem-CEDS (abbreviated as CAM-CEDS above) for 4°-wide latitude bins centered at (a) 12°N and (b) 12°S. The thick solid lines represent the mean values from MLS (black), WACCM (red) and CAM-chem-CEDS (blue), with corresponding variability estimates (twice the standard deviations) given by the colored dashed lines about each mean.



1355
1356
1357
1358
1359
1360
1361

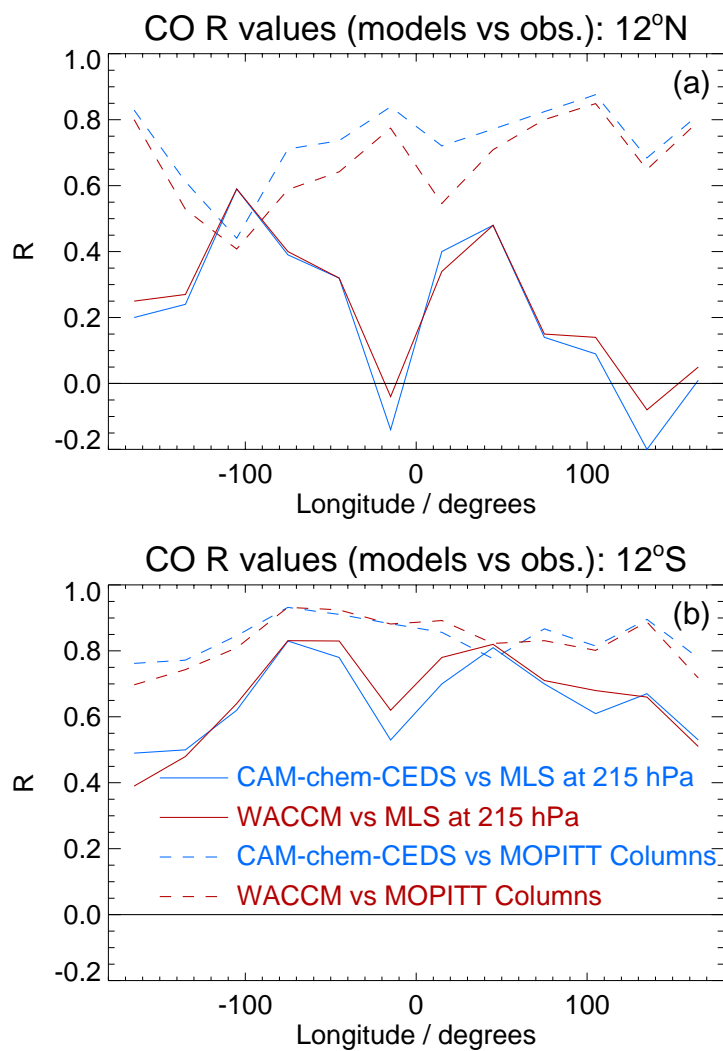
Figure 10. CO column comparisons between zonal mean time series from MOPITT (purple) X_{CO} (see text) and from CAM-chem-CEDS (blue) and WACCM (red) for 4°-wide latitude bins centered at (a) 12°N and (b) 12°S.



1362

1363

1364



1365

1366

1367

1368

1369

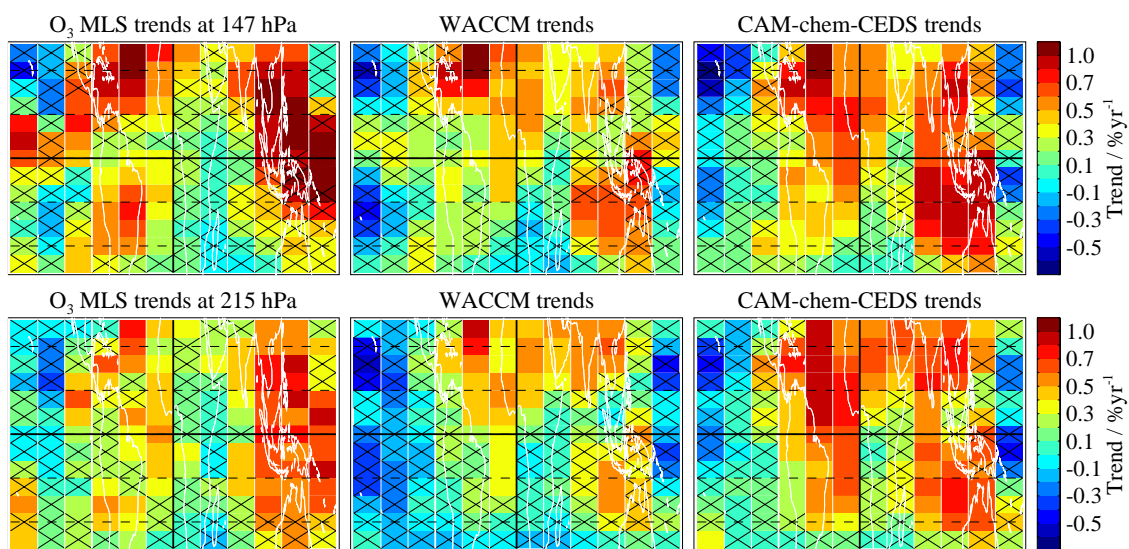
1370

1371

1372

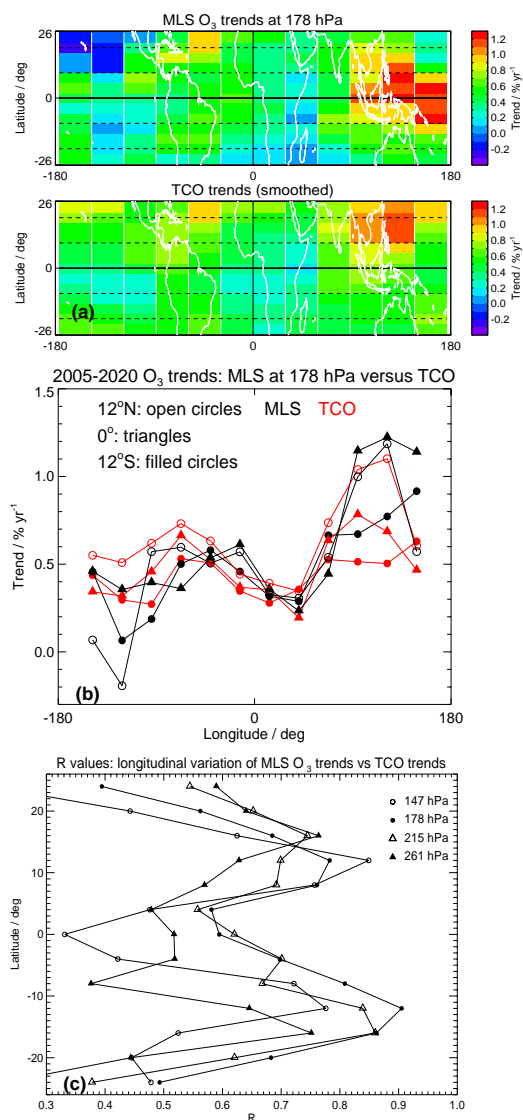
1373

Figure 11. Correlation coefficient values (R) for the zonal mean time series from the model CO columns (CAM-chem-CEDS in blue, WACCM in red) versus MOPITT columns (dashed) and from the same two models' CO mixing ratios versus MLS CO at 215 hPa (solid) for 4°-wide latitude bins centered at (a) 12°N and (b) 12°S.



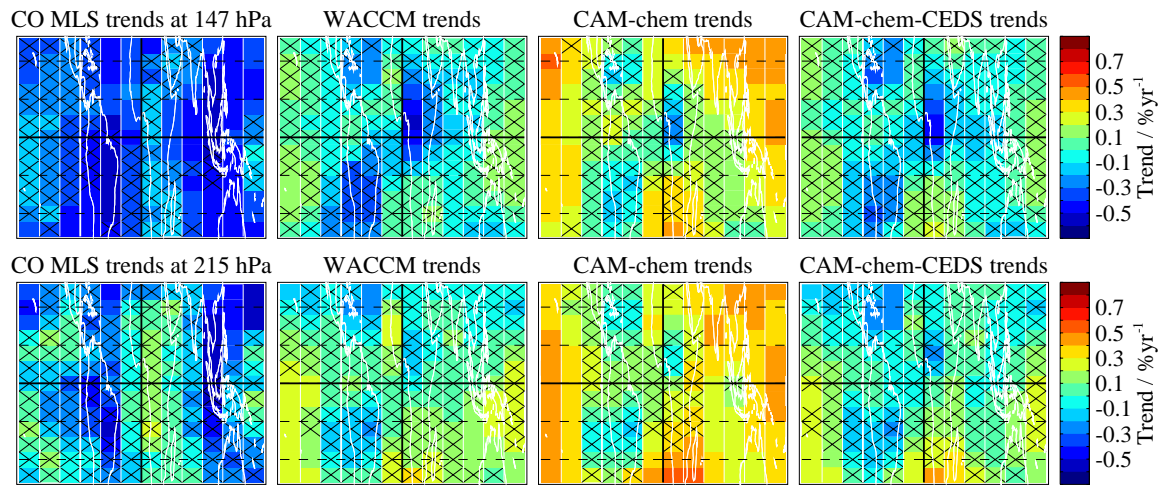
1374
1375
1376
1377
1378
1379
1380
1381
1382
1383

Figure 12. Maps of upper tropospheric O₃ trends (% yr⁻¹) in the tropics for 147 hPa (top row) and 215 hPa (bottom row); the latitude range is from 26°S to 26°N, with maps all centered on the Greenwich meridian. MLS trends (left column) are compared to trends from WACCM (middle column) and CAM-chem-CEDS (right column). Black crosses show grid boxes for which the trend estimate is not significantly different from zero (based on our 2σ error estimates).



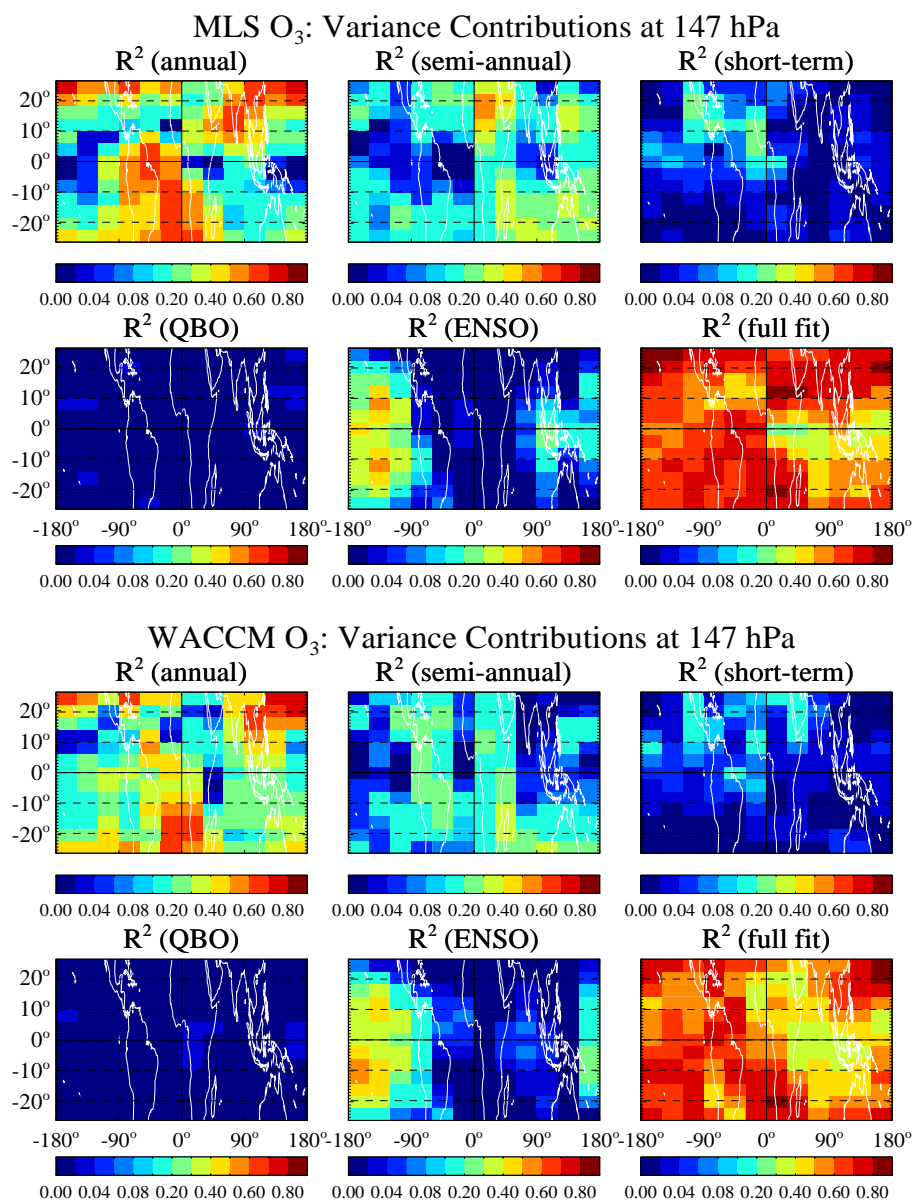
1384
1385
1386
1387
1388
1389
1390
1391
1392
1393
1394
1395
1396

Figure 13. (a) The top map shows MLS ozone trends (2005–2020) at 178 hPa and the bottom map displays horizontally-smoothed tropospheric column ozone trends for the same time period, following the analyses of Ziemke et al. (2019) (b) cross sections of the above mapped trends in 4°-wide latitude bins centered at 12°N, 0°, and 12°S (see legend) for MLS (black) and TCO (red), (c) correlation coefficient values R (on the x axis) between the MLS ozone trends at different pressures (see legend) and the TCO trends as a function of longitude, at different tropical latitudes (y axis). This panel provides a broader picture of the trend correlations, which exhibit a minimum near the Equator and maxima near 12°S and 12°N.



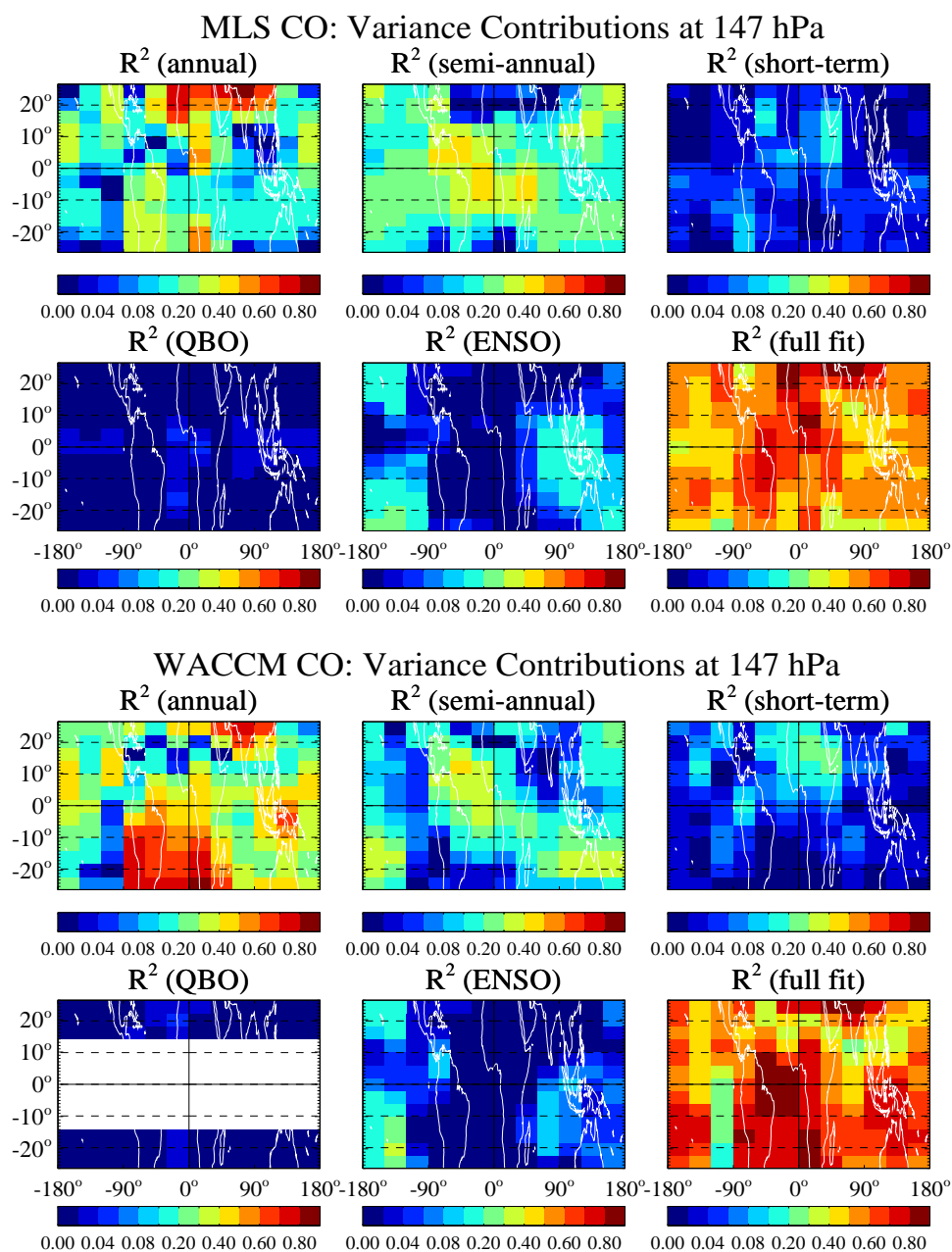
1397
1398
1399
1400
1401
1402

Figure 14. Same as Fig. 12, but for CO trends and three model results.



1403
1404
1405
1406
1407
1408
1409
1410
1411
1412
1413

Figure 15. Contributions to the time series variance from the main fitted components of the regression to the gridded tropical MLS ozone time series at 147 hPa (top 8 panels) and the same for the WACCM time series (bottom 8 panels). The titles in each panel indicate that the explained variance is from specific components (annual, semi-annual, short-term, QBO, ENSO, and full fit).

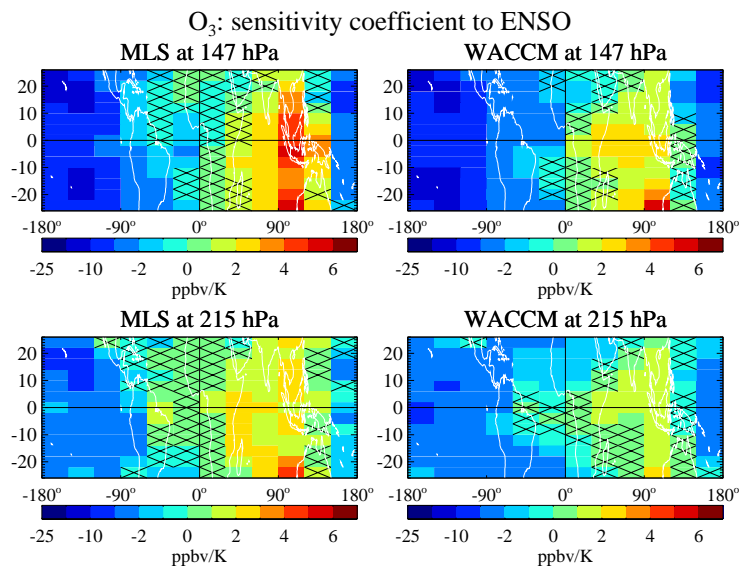


1414
1415
1416
1417

Figure 16. Same as Fig. 15, but for CO.



1418
1419
1420

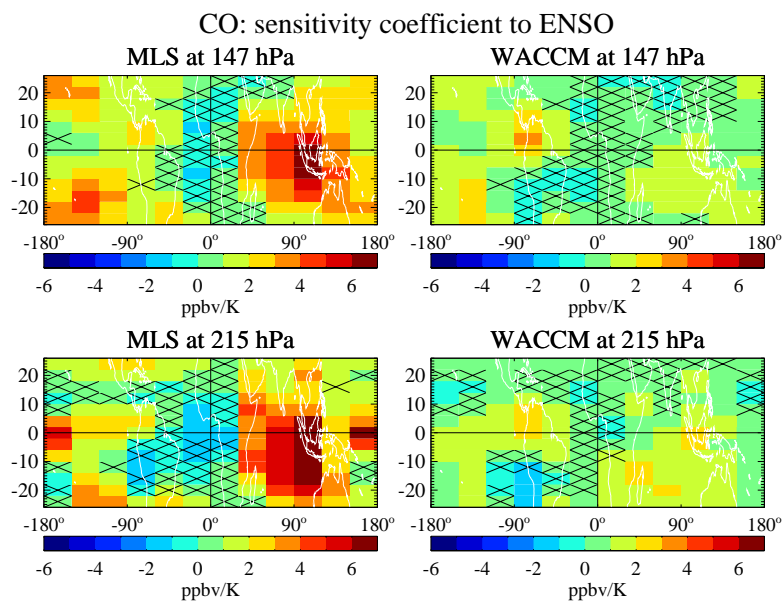


1421
1422
1423
1424
1425
1426
1427

Figure 17. Sensitivity coefficient to ENSO for ozone at 147 hPa (top panels) and 215 hPa (bottom panels); MLS results are shown in the left panels and the WACCM results in the right panels. The black crosses show the grid boxes for which the sensitivity is not significantly different from zero (based on the 2σ error estimates).



1428
1429
1430



1431
1432
1433
1434
1435

Figure 18. Same as Fig. 17, but for CO.